Contact mechanical measurements under high frequency oscillation

Dissertation

zur Erlangung des Grades eines Doktors
der Naturwissenschaften

vorgelegt von
Sergiy Rudenkiy
aus Kharkiv (Ukraine)

genehmigt von der Fakultät für Natur- und Materialwissenschaften
der Technischen Universität Clausthal
Tag der mündlichen Prüfung
16 Nov. 2007

Vorsitzender der Promotionskommission

Prof. Dr. W. Schade

Hauptberichterstatter

Prof. Dr. D. Johannsmann

Berichterstatter

Priv.-Doz. Dr. Jörg Adams

angefertigt am

Institut für Physikalische Chemie

Technische Universität Clausthal

Arnold-Sommerfeld-str. 4

38678 Clausthal-Zellerfeld

Hiermit erkläre ich an Eides Statt, dass ich die bei der Fakultät für Material- und Naturwissenschaften der Technischen Universität Clausthal eingereichte Dissertation selbständig und ohne unerlaubte Hilfe verfasst und die benutzten Hilfsmittel vollständig angegeben habe.

Datum: Unterschrift

Acknowledgment

At this place I would like to say thanks to all people who have contributed directly or indirectly to the success of this dissertation.

I would like to sincerely thank my research advisor, Professor Dr. Diethelm Johannsmann.

First part of my work was done with the help of Dr. B. Du. I would like to thank him for the team-work in the labor. I would also like to thank Johanna Bünsow and Kerstin von der Ehe for the funny atmosphere in the office during my sty in IPC TU-Clausthal. Also thanks them and all other peoples from the group of prof. Dr. Diethelm Johannsmann for the powerful discussion of my work during group seminars.

Thanks for the discussions and cooperation with all of my colleagues have contributed substantially to this work. Thanks for all institutes coworker for the nice time in IPC TU-Clausthal.

Thanks to the workshop workers and actually Mr. Cronjäger for the all things I need to build during my PhD work.

I dedicate this thesis to my father and mother.

Abstract

Micromechanical contacts between a spherical surface and a solid plane have been investigated with acoustic resonators. The elastic stiffness of the contact as well as the static friction coefficient have been inferred from the shifts of frequency and bandwidth of the resonator as a function of shear amplitude. In the limit of small amplitudes, the shifts of frequency and bandwidth, Δf and $\Delta\Gamma$, are well described by the Mindlin model. The frequency shift (that is, the apparent spring constant) decreases linearly with shear amplitude. From the intercept with the ordinate and the slope, one infers the spring constant and the static friction coefficient, respectively.

When employing very high levels of oscillatory shear stress, one irreversibly changes the stiffness of the contacts. Both a weakening and a strengthening can be found, depending on the conditions.

Increasing the environmental humidity leads to the formation of capillary bridges and menisci in the area of contact. The capillary forces increase the stiffness of the contacts. Further, the liquid acts as a lubricant, decreasing the static friction coefficient. The contact strength strongly increases when the sample returns to the dry state after having been exposed to high humidity. The effect is termed “hysteretic sandcastle effect”. It is explained by a deformation of the two surfaces under the influence of the Laplace pressure. Further application of high-frequency oscillatory stress can reverse this effect (that is, disrupt the bonds formed during the dry–humid–dry cycles). Larger contacts tended to be more stable against this shear-induced removal of the sandcastle effect than smaller ones.

Measurements of the adhesion force between AFM-cantilevers and the surface of acoustic resonators covered with mica showed a strong decrease of the pull-off force with shear amplitude. Similar results were found in colloidal probe experiments, where a glass sphere was glued to the cantilever. Three regimes were identified, which consisted of two plateaus at very low and high amplitudes and an intermediate range, characterized by a logarithmic decrease of the pull-off force with amplitude. The logarithmic dependence on amplitude suggests that thermally activated processes govern the detachment dynamics.

Zusammenfassung

Gegenstand der Untersuchung war der mikromechanische Kontakt zwischen einer sphärischen und einer ebenen Oberfläche mittels akustischen Resonatoren. Die elastische Steifigkeit des Kontakts sowie der statische Reibungskoeffizient wurden aus den Verschiebungen von Frequenz und Bandbreite des Resonators als Funktion der Scheramplitude erschlossen. Im Grenzfall kleiner Amplituden lassen sich Bandbreiten- und Frequenzverschiebung, $\Delta\Gamma$ bzw. Δf, gut durch das Mindlin-Modell beschreiben. Die Frequenzverschiebung (die scheinbare Federkonstante) nimmt linear mit der Scheramplitude ab. Aus dem Ordinatenabschnitt lässt sich die Federkonstante und aus der Steigung der statische Reibungskoeffizient bestimmen.

Werden hohe oszillatorische Scherspannungen angelegt, wird die Steifigkeit der Kontakte irreversibel verändert. Je nach Bedingungen findet man eine Ab- oder Zunahme der Steifigkeit.

Erhöhung der Luftfeuchtigkeit führt zur Bildung von Kapillarbrücken und Menisken an der Kontaktfläche. Die Kapillarkräfte führen zu einer Zunahme der Kontaktsteifigkeit. Außerdem wirkt die Flüssigkeit als Schmiermittel, was den statischen Reibungskoeffizienten senkt. Die Kontaktsteifigkeit steigt stark an, wenn ein zunächst der Feuchtigkeit ausgesetzter Kontakt wieder eintrocknet. Dieser Effekt wurde als „hysteretischer Sandburg-Effekt“ (hysteretic sandcastle effect) bezeichnet. Er lässt sich durch Deformation der Kontaktstellen aufgrund des Laplace–Drucks erklären. Weitere Einwirkung hochfrequenter Scherfelder kann diesen Effekt umkehren, also die Bindungsstellen wieder trennen, die sich während der Trocken–Feucht–Trocken–Zyklen gebildet haben. Größere Kontaktflächen erwiesen sich als stabiler als kleine gegenüber diesem scherinduzierten Abbau des Sandburg-Effekts.

Messungen der Adhäsionskraft zwischen einem AFM-Cantilever und der Oberfläche von akustischen Resonatoren, welche mit Glimmer beschichtet waren, zeigten eine starke Abnahme der Abreißkraft mit zunehmender Schermplitude. Ähnliche Ergebnisse zeigten Versuche mit kolloidal modifizierten Sonden, bei denen eine Glaskugel an der Cantileverspitze befestigt wurde. Drei Bereiche ließen sich unterscheiden: zwei Plateaus bei sehr kleinen und großen Amplituden sowie ein mittlerer Bereich, der sich durch einen logarithmischen Abfall der Abreißkraft mit der Scheramplitude auszeichnet. Die logarithmische Abhängigkeit legt nahe, dass thermisch aktivierte Prozesse die Dynamik der Ablösung bestimmen.

Table of contents

1. Introduction

Friction between solid surfaces is of outstanding importance in many areas of science and engineering. The first study of the friction was carried out by Leonardo daVinci about five centuries ago [1, 2, 3, 39]. Later, in the 17th century Guillaume Amontons phrased two basic empirical laws of sliding friction. Friction is proportional to the applied normal force and friction is independent of the contact area of the sliding surfaces. One century later Charles Augustin de Coulomb introduced the third empirical law, namely that the friction force is independent of the sliding velocity. Together, these three 'laws' are known as the Amontons–Coulomb laws of sliding friction. They can be described with the simple equation $\mu = F/N$, where μ is the constant or friction coefficient, F is the applied force, and N is the normal load [4].

In the Amontons–Coulomb law, friction is independent of the area of contact. It depends only on the load. It is a consequence of the fact that for most practical surfaces the average contact area increases linearly with the applied normal force [5]. Bowden and Tabor have expressed the friction force as a function of real contact area [6]. The real area of contact between solid surfaces is much smaller than the apparent contact.

Further investigations of the friction is became possible with new technique like Atomic Force Microscopy (AFM), the Surface Forces Apparatus (SFA), and the Quartz Crystal Microbalance (QCM). AFM is characterized by atomic-scale length measurements, slow sliding or long time scales, and high shear stress [7]. With an AFM, it is possible to measure lateral force exerted by a single atom at a sharp tip. The SFA was first developed by Bowden and Tabor in the 1950´s and later adapted for friction measurements. The SFA covers comparatively long length and time scales and medium range stresses [8]. The use of the QCM in tribological measurements was first demonstrated by Jacqueline Krim and co-workers [7, 9, 10]. This technique is accurate enough to measure forces down to the atomic scale. The QCM covers atomic length scales, short time scales and low shear stress.

The idea that fiction is related to the bonding energy between surfaces was expressed by Zhong et al [11]. The friction coefficient also depends on the adsorption energy and the adhesion between the solid surfaces. The adhesion energy is affected by long range forces in addition to the force acting right at the surface. Plastic deformation also plays some role. This statement is valid in a wide range of experiments.

In order to investigate the force of adhesion between surfaces and nano-asperities, the AFM is widely used [12, 13]. The sharp tip of the AFM-cantilever makes it difficult to quantify the relation between contact area and friction at the nanoscale. An alternative it to use small clusters materials with defined shape mounted to the AFM-cantilever [14, 15].

Finally, recent theoretical investigation for the continuum mechanics can not be applied to nanometer-sized contacts. Continuum theory brakes down at atomic scale [16]. When placing two solid surfaces in contact and sliding them over each other, the total force of friction is the outcome of a number of different physical phenomena. There is elastic deformation, adhesion, wear, and others. Each of these phenomena plays its own role and depends differently on the area of contact.

There are several motivations to study tribology on the nanoscale and at high frequency. Using the QCM in our investigation, we try to understand the phenomena of friction and adhesion that take place under high frequency oscillatory shear and on short time scales. This work is not concerned with the nanotribology in sense of single contacts. In our investigation we have used multi-asperity contacts between an assembly of the spheres and a plate. It is also known that the presence of the lubricant has a large influence on friction. Sometimes, small volumes of the water can play the role of lubricant. Condensation of water plays a significant role in friction phenomena. For this reason, it is also interesting to investigate friction and adhesion in high humidity.

To analyze the data from the QCM experiments we use the Mindlin model [17]. This model describes stick–slip transition in the Hertz contact under oscillatory force. It involves partial slip at the rim of the contact area.

2. Fundamentals of contact mechanics

2.1. Introduction

The aim of this part is to provide a short review of the current knowledge in the field of contact mechanics. The subject of contact mechanics may be said to have started with the work of Heinrich Hertz.

Section 2.2 shortly introduces Hetrz studies in field of contact between two elastic half-space spheres. In section 2.3, we will talk about the nature of adhesion between bodies. Section 2.4 will describe more in detail meniscus forces or capillary forces. These forces play a significant role in adhesion and friction. The presence of liquid menisci in the contact increases the adhesion force between the bodies. In our experimental results, we will show that capillary forces increase the real area of contact between two bodies. In section 2.5, we will discuss some aspects of the friction forces. For microscopic surfaces, we have a dependence of the friction force on the area of contact. Therefore, menisci in the contact will increase the real area of contact and increase the friction force. On the other hand, they can also act as lubricants.

2.2. Hertz theory of elastic contact

In 1889 Hertz started his work on mechanics. He had studied interference of the light passed through two cylindrical lenses in contact. After five years of experimental and theoretical work he published his book *"Die Prinzipien der Mechanik in neuem Zusammenhange dargestellt"*, in 1894.

In this work, Hertz solved the problem of two elastic spheres pushed against each other. The expression "elastic spheres in contact" means that we have two elastic bodies whose deformation is small in comparison with the linear size of the bodies. In the case of spheres, this implies that the deformation is small compared to the radii of curvature of the undeformed surfaces. The contact stresses are highly concentrated at the region of contact. The size of the bodies is larger than the contact area and there is no influence of the stress on to the volume elements distant from the contact. In Hertz theory we neglect the tangential displacements produced by the contact pressure [76].

In the general case, we have two elastic spheres with radii R_1 and R_2. The surfaces of these spheres are frictionless. Without applied pressure the spheres are in contact (Fig. 1*a*). Under a vertical force, *P*, the contact area is displaced by some values $u_1(r)$ and $u_2(r)$ for the first and the second sphere, respectively. The centers of the two spheres approach each other by a distance δ and contact is achieved on a circle with radius *a* (Fig. 1*b*).

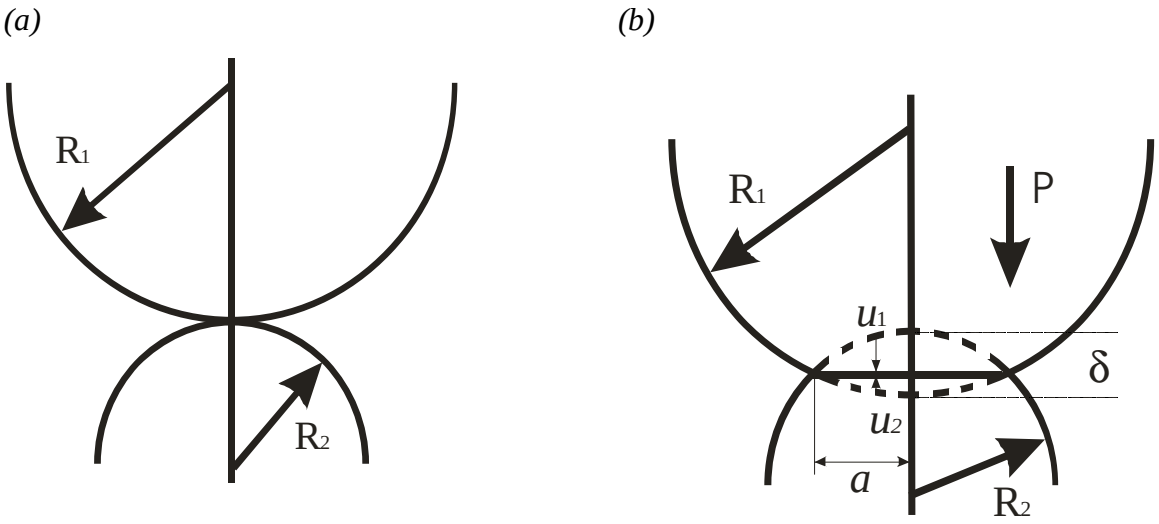

Fig. 1. Two spheres in single point contact (a) and under vertical pressure (b)

The boundary conditions for the displacement in the area of contact can be written as

$$u_1(r)+u_2(r)=\delta-\left(\frac{1}{2R}\right)r^2,\ r\le a \qquad \text{Eq. 2.1}$$

where $1/R=1/R_1+1/R_2$ is the mean curvature.

The dependence of contact radius on the force in Hertz theory can be written as

$$a^3=\frac{3PR}{4E} \qquad \text{Eq. 2.2}$$

where the effective Young modulus is given as

$$\frac{1}{E}=\frac{1-\nu_1^2}{E_1}+\frac{1-\nu_2^2}{E_2} \qquad \text{Eq. 2.3}$$

The value of *a*, can be calculated for known parameters of *P*, *R*, and *E*. This value is termed “Hertz radius”, R_{Hertz}, in the results section (see, for example, Table 1 in section 4.3).

In Eq. 2.3, E_1, E_2, ν_1 and ν_2 are Young's moduli and Poisson ratios for the first and second body, respectively. The indentation δ of the two solids is given by

$$\delta = \frac{a^2}{R} = \left(\frac{9P^2}{16RE^2} \right)^{1/3} \qquad \text{Eq. 2.4}$$

The distribution of the pressure is

$$p = p_0 \left\{ 1 - \left(\frac{r}{a} \right)^2 \right\}^{1/2} \qquad \text{Eq. 2.5}$$

where p_0 is the maximum pressure in the centre of contact given by

$$p_0 = \frac{3P}{2\pi a^2} = \left(\frac{6PE^2}{\pi^3 R^2} \right)^{1/3}. \qquad \text{Eq. 2.6}$$

When we have a contact between a sphere and a surface, ($R_2 \rightarrow \infty$, $E_2 >> E_1$) we have

$$\frac{1}{E} = \frac{1-\nu_1^2}{E_1} \qquad \text{Eq. 2.7}$$

The relation between the applied load and the approach distance, δ, is

$$\delta = const \cdot P^{2/3}, \; P = const \cdot \delta^{3/2} \qquad \text{Eq. 2.8}$$

This result is true for the bodies of different shape.

2.3. Adhesion

The adhesion force between a sphere and a smooth surface is a fundamental problem in engineering. Particle adhesion is controlled by dispersive forces (JKR model of elastic contact [18]), local chemical bonding, charge, and capillary attraction. These forces are strongly affected by surface properties like roughness and surface chemistry.

The JKR model deals with the interaction caused with the Van der Waals (vdW) forces. This interaction is always presented and cannot be removed. To describe the attractive force of the deformable spherical particles, Johnson et al. [18, 19] extended Hertz theory of elastic contact. They find that

$$F_{JKR} = \frac{3}{2}\pi R\gamma \qquad \text{Eq. 2.9}$$

where R is equivalent radius and γ is the interfacial energy. Eq. 2.9 is applies in the absence of a load.

Charge or electrostatic forces are due to the electricity phenomena. Electrostatic forces arise when two surfaces electrically charged.

The capillary force is an attractive force that arises from the Laplace pressure (Eq. 2.11) of curved menisci between the two surfaces. The menisci form as a result of condensation of vapor in the environment of the surfaces. The capillary condensation of some liquids, most notably water, gives rise to adhesion force in the contact zone. More details on the capillary force will be discussed in the next section.

2.4. Capillary forces

For simplicity this section we mostly deal with water vapors, but most of the statements hold for other liquids, as well. Menisci on the contact can be formed, if the radius of curvature of the micro contacts is below a certain critical radius [21]. This radius is approximately equal to the Kelvin radius. Lord Kelvin derived the relationship between the vapor pressure of a liquid, P, and mean radius of curvature, r_K, of the liquid vapor interface [22, 26, 27]:

$$r_K = -\frac{\gamma V_M}{RT\ln(\frac{P}{P_s})} \qquad \text{Eq. 2.10}$$

where V_M is the molar volume of the liquid, γ is the surface tension, R is the universal gas constant, T is the temperature, and P_s is the saturation vapor pressure. For water at room temperature, the surface tension is $\gamma = 0.074$ N/m, the molar volume is $V_M = 18\ 10^{-6}$ m^3 mol^{-1}, the universal gas constant is $R = 8.31$ m^3 Pa mol^{-1} K^{-1}, and the temperature is $T = 300$ K. For $P/P_s \sim 0.9$, we obtain Kelvin radius of about 5 nm.

The capillary forces are well studied in the works of Young, Laplace, and Kelvin. The additional pressure due to the curvature radius of the menisci is described by the Laplace pressure [23, 24]

$$\Delta p = \gamma\left(\frac{1}{R_1}+\frac{1}{R_2}\right) \qquad \text{Eq. 2.11}$$

where R_1 and R_2 are the radii of curvature for the menisci. For a long time, a very simple equation has been used to describe capillary forces [24, 25, 76]

$$F_c = 2\pi R_s \gamma(\cos\theta_1 + \cos\theta_2) \qquad \text{Eq. 2.12}$$

In this equation R_s is the radius of the sphere, θ_1 and θ_2 are the contact angles. This equation applies to equilibrium state, when perfectly smooth surfaces stay in contact for a long time. This model does not take roughness of the surfaces and a dependence of the capillary force, F_c, on the relative humidity into account. If the contact time is below a critical time, it has been observed that the capillary force increases with time [30, 32]. Investigations of the adhesion force show a dependence on the normal load [31], which is not described by Eq. 2.12. Recent investigations also show a dependence of the capillary force on humidity and surface roughness [28, 29, 30]. Fig. 2*a* shows an illustration of the sphere plate contact in high humidity. The Hertzian contact is carried by small asperities. Near these small asperities, menisci form. In the points where the distance between surfaces is less than two Kelvin radii, water bridges form. Fig. 2*b* shows water bridges with the Kelvin radii of curvature. This assumption explains the increase of the capillary force with humidity and contact time. Assuming that the number of microcontacts increases with load can explain the dependence of the adhesion force on the normal load.

Taking the roughness of the surface into account, we can modify Eq. 2.12 for the total capillary force [22]

$$F_c \cong 2\pi R_a \gamma(\cos\theta_1 + \cos\theta_2) N_c \qquad \text{Eq. 2.13}$$

where N_c is the number of capillaries formed and R_a is the average radius of the asperities. The number of contacts increases with time of contact and relative humidity. This number also depends on the total number of asperities, where it is possible to form capillaries. This total number can be calculating using the Hertz theory of elastic contact. Finally, we obtain the following the relationship for the capillary force [22]

$$F_c \cong \frac{8\pi\gamma}{R_a}\left(\cos\theta_1 + \cos\theta_2\right)\left(\frac{V_M}{\lambda R_c^2}\right)\frac{\ln\dfrac{t}{t_A}}{\ln\dfrac{P_s}{P}}\left(r_K R_s + R_{Hertz}^2\right) \qquad \text{Eq. 2.14}$$

where V_M is the molar volume of the liquid, R_c is the average radius of one capillary, λ is the full width at half-maximum of the interstitial height distribution [30, 32], t_A is the condensation time of a liquid monolayer, P_s is the saturated vapor pressure, r_K is the Kelvin radius calculated from the Eq. 2.10, R_s is the radius of the sphere in contact with surface, and R_{Hertz} is the Hertz radius of contact calculated with Eq. 2.2.

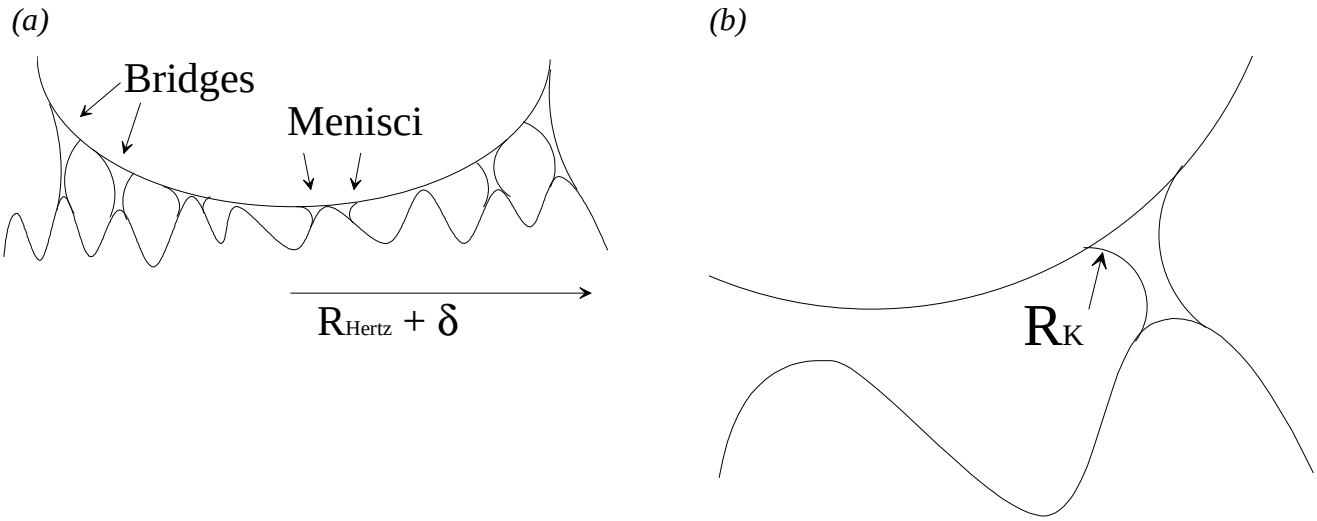

Fig. 2. Illustration of the sphere plate contact in high humidity. (a) Contact between sphere and plate carried by small asperities. In the points of contact we have menisci. When the distance is comparable to the Kelvin radius, (b) water bridges form.

2.5. Friction

Two macroscopic solids in contact exhibit a resistance to relative motion. The resistance to the motion is known as friction. Friction force are nonconservative, converting kinetic energy to internal energy. Friction between the macroscopic surfaces is well described by the Amontons–Coulomb law

$$\mu = \frac{F}{N} \qquad \text{Eq. 2.15}$$

where F is the frictional force, μ is friction coefficient, and N is the load normal to the surface. This model does not depend on the area of contact or adhesion. A real contact between two surfaces is made across many small asperities. The nature of the friction

between these small asperities is rather different from macroscopic friction as by the Amontons–Coulomb law.

Bowden and Tabor [39] have modified the classical Amontons–Coulomb friction law. They define friction force as the product of a critical stress, σ_s, and the real area of contact, Σ_r

$$F = \sigma_s \Sigma_r \qquad \text{Eq. 2.16}$$

Following to the Greenwood–Williamson [5, 82, 89] model, the real area of contact is proportional to the normal load. There are others models describing friction phenomena. These take phonon friction (Tomlinson) and electronic friction into account.

In the Tomlinson model [20] friction occurs due to the vibration of the atomic lattice. The atoms close to surface vibrate when the atoms of the opposite surface slip across. These phonons dissipate energy, which leads to friction.

Electronic friction can also contribute to the friction force [33, 34, 35, 36, 37]. The electronic mechanism involves energy transfer to the conduction electrons. Sliding across a metal substrate causes excitations of the conduction electrons near the interface. The excitations generate electron–hole pairs. These pairs have very short lifetimes in metals. When these electron–hole pairs recombine, the excess energy is dissipated as heat.

In order to initiate sliding it is necessary to exert a force. The force that we need to initiate the sliding is known as the static friction force. This force usually is large than the one required to keep the surfaces in motion. However, in this situation partial slip occurs. The region of the slip is confined to the edge. In the central part of the contact we have stick [42].

A phenomenon closely correlated to the static friction is “stick–slip” friction. This term was first used by Bowden and Tabor [39], when described the relative motion of two surfaces in the contact. They noted that the motion is controlled by the kinematic friction law often the surfaces have started slipping. On the contrary, the motion is described by static friction when the surfaces stick. However, when the relative motion is slow (for example when an oscillatory motion changes direction) it is necessary to review static and kinematic models and brings them to a synthesis. Atomic-scale stick–slip friction was first measured with an AFM by Mate et al. in 1987 [38]. Since 1987, atomic scale stick–slip friction for different materials has been observed.

One of the phenomenological theories of the transition from stick–slip motion to smooth sliding is based on the assumption that the static friction force depends on time [78, 79, 80, 81]

$$F_s = F_{s1} + \left(F_{s2} - F_{s1}\right)\left(1 - e^{-t/\tau}\right) \qquad \text{Eq. 2.17}$$

At $t = 0$, the frictional force is equal to F_{s1}, but later, it approaches the value F_{s2} ($t \to \infty$). τ is characteristic time. Following to the BT friction law, we can assume that the real surface area increases with the time of contact. Assuming that the critical stress is independent of the time of the contact, one estimates the real area as

$$\Sigma_r = \Sigma_{r1} + \left(\Sigma_{r2} - \Sigma_{r1}\right)\left(1 - e^{-t/\tau}\right) \qquad \text{Eq. 2.18}$$

where, Σ_{r1} is the area of contact in the moment when two surfaces placed in contact and Σ_{r1} is the area after a waiting time.

3. The Quartz Crystal Microbalance (QCM)

3.1. Introduction

Pierre and Marie Curie showed in 1880 that crystal of Rochelle salt could produce electricity when pressure was applied [45, 46, 47]. Later, the opposite effect was demonstrated, as well. The crystal produces a strain upon application of an electric voltage. These findings were the discovery of the piezoelectric effect. Initially this effect did not receive much interest. In 1917, almost forty years after its discovery, Paul Langevin developed the first application of the piezoelectric effect when he constructed an underwater ultrasonic detector.

Further developments of the quartz crystal devices started in 1934, when the AT-cut quartz crystal was introduced. The advantage of the AT-cut is that it has nearly zero frequency shift drift with the temperature around room temperature. In 1959 Sauerbrey published a paper which showed that the frequency shift of a quartz crystal resonator is directly proportional to the added mass [48]. Sauerbrey work discovered a new quantitative tool to measure very small masses.

Nowadays the quartz crystal microbalance (QCM) is a well-known and widely used instrument to measure film thickness in the nanometer range. However, the quartz crystal responds to many other physical parameters such as temperature, stress and viscosity. We use the term QCM in all these applications, even when the device is not used as a balance. The QCM can be combined with the other technique such as cyclovoltammetry [53], surface plasmon resonance spectroscopy [49, 50], atomic force microscopy [51, 52], and others. The QCM can be found in different areas of the science such as biotechnology, functionalized surfaces, thin film formation, surfactant research, drug research and contact mechanics (Fig. 3).

This work is mainly concerned with the application of the QCM in contact mechanics measurements. The first part concerns with the interaction of the quartz crystal with discrete objects. The second part deals with adhesion force measurements via the investigation of the pull–off–distance under high frequency oscillatory shear of the quartz crystal. Here, the QCM plays the role of an oscillator with a well defined shear amplitude.

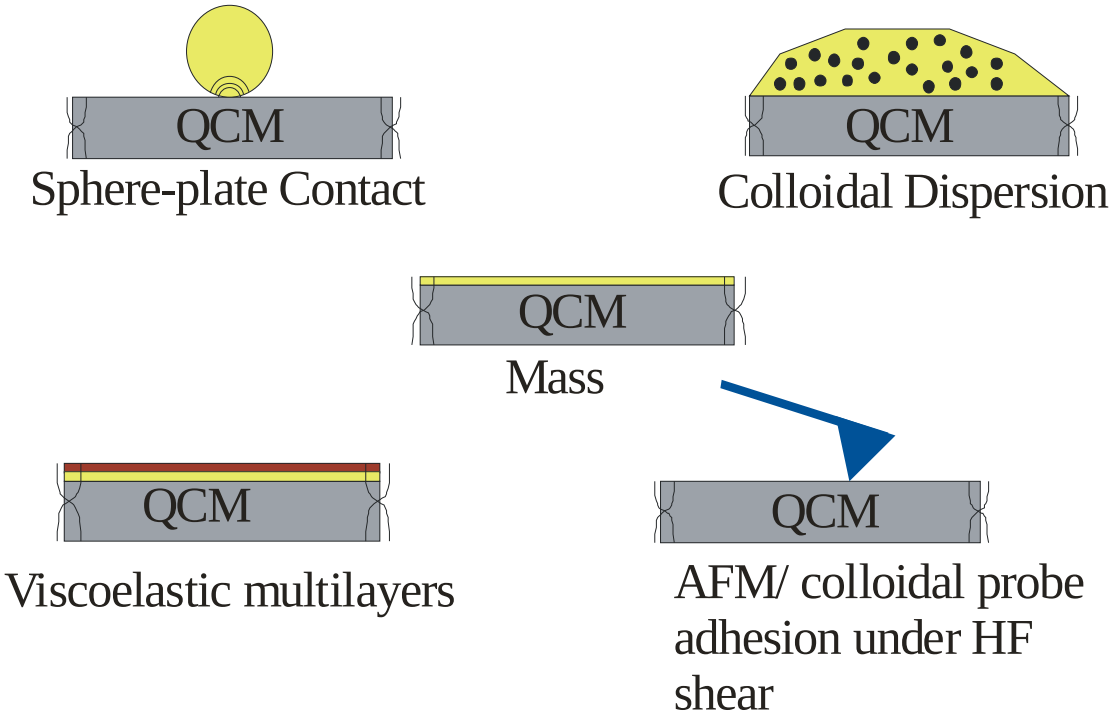

Fig. 3. Different applications of the QCM.

3.2. Complex resonance frequency

With impedance analysis, one determines the frequency, *f*, and the Half–Band–Half–Width (HBHW), Γ. In this work, the HBHW is termed "bandwidth". One can define a complex resonance frequency $f^* = f_0 + i\Gamma$, where the real part is the resonance frequency and the imaginary part is the bandwidth of the resonance. Loading of the crystal leads to the frequency shift, $\Delta f^* = f^* - f^*_0$, relative to unloaded quartz (*Fig. 4*). For the complex resonance frequency, the small load approximation holds [64]:

$$\frac{\Delta f^*}{f_0} = \frac{\Delta f + i\Delta\Gamma}{f_0} \approx \frac{iZ^*}{\pi Z_q} = \frac{i\sigma}{\pi Z_q \, \partial u / \partial t} \qquad \text{Eq. 3.1}$$

with the frequency shift, Δf, and the bandwidth shift, $\Delta\Gamma$. $Z_q = 8.8\ 10^6$ Kg m^{-1} s^{-2} is the acoustic impedance of the AT-cut crystal. Z^* is the load impedance defined as

$$Z^* = \frac{\sigma}{\partial u / \partial t} \qquad \text{Eq. 3.2}$$

where σ is the shear stress and *u* is displacement at the quartz–sample interface. This formula for the frequency shift holds for small frequency shifts and, as a consequence, for small loads.

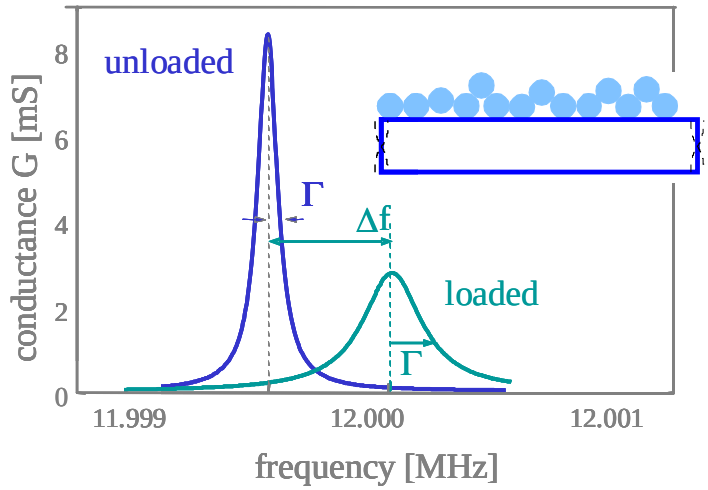

Fig. 4. Bringing an acoustic resonator into contact with an assembly of small spheres increases its frequency and its bandwidth.

As Eq. 3.1 shows, the QCM measures a stress–speed ratio. The small load approximation it is a quantitative model to describe frequency shift induced by stress at the quartz–sample interface. Before using this model, we need to explain, what the quartz–sample interface is. For a semi-infinite sample, load impedance is simply the acoustic impedance of the respective materials $(G\rho)^{1/2}$ with G the shear modules and ρ the density of the sample.

The bandwidth, Γ, is used to describe dissipation of the system. Other common parameters are the quality factor, Q, and the dissipation $D = Q^{-1}$. Q is defined as

$$Q = \frac{f_0}{2\Gamma} \qquad \text{Eq. 3.3}$$

Eq. 3.1 is the most important equation in the physics of QCM. For small frequency shifts ($\Delta f << f_0$), the complex frequency is proportional to the load impedance at the crystal–sample interface. The frequency shift depends on the stress–speed ratio at the crystal surface. There are many non planar samples like sand, spheres, droplets, or other heterogeneous materials. For these samples, the small load approximation under certain conditions can also be applied, using an *average* stress. The frequency shift for such systems can be estimated from the average ratio of stress and speed at the crystal–sample interface.

3.3. The Butterworth-van-Dyke electromechanical equivalent circuit

An equivalent circuit is a simple graphical representation of the QCM. In physics, scientists often deal with the different kinds of waves. These can be electrical or mechanical waves. The easiest resonator in electronics consist of a capacitance, a resistor and a inductance placed in the series. To describe such system we need to use the Kirchhoff laws.

In mechanics, the equivalent elements for the capacitor, the inductance and the resistor are the spring, the mass and the dash pot. The ratio of force and speed (speed of the displacement) is the mechanical impedance.

Using equivalent circuits, we can understand how acoustic phenomena can be described with the electrical circuit. The force is represented by a voltage and the speed by a current. The ratio of force and speed is the mechanical impedance.

When representing mechanical elements with equivalent electrical circuits, elements which are placed in series, have to be drawn in parallel in the equivalent circuit. For two parallel elements in the electrical circuit current (speed in mechanics) is additive. Consequently, for two mechanical elements connected in parallel, we draw the electrical elements in series. For parallel electrical elements the voltage (force in mechanics) is additive (Fig. 5). Drawing mechanical elements in equivalent circuits we can use Kirchhoff laws to calculate forces, speeds, resonance frequencies and all other circuit parameters..

(a) Mechanical situation *(b) Equivalent circuit*

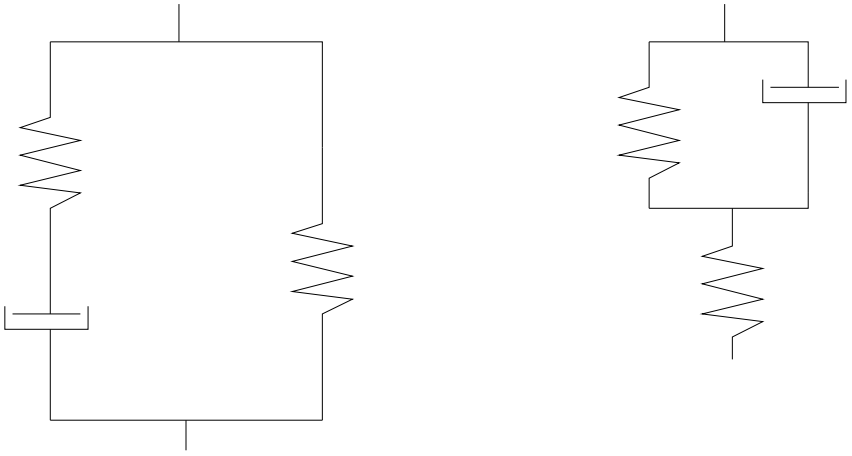

Fig. 5. Representation of the mechanical (a) situation with equivalent circuit (b)

Close to the resonance the crystal can be approximated by a resistor, a capacitor and a inductance (“BvD–circuit”) [62, 63, 83]. Fig. 6 shows the BvD equivalent circuit for the

unperturbed quartz crystal resonator. The components are related to the properties of the QCM as follows: R_1 represents the losses in energy due to the viscous damping of the oscillation in the surrounding medium, C_0 is related to the capacitance of the electrodes deposited on the surfaces of the crystal disc, C_1 is related to the elasticity of the crystal (the oscillation energy stored in the crystal), and L_1 corresponds to the inertial component of the oscillation [54].

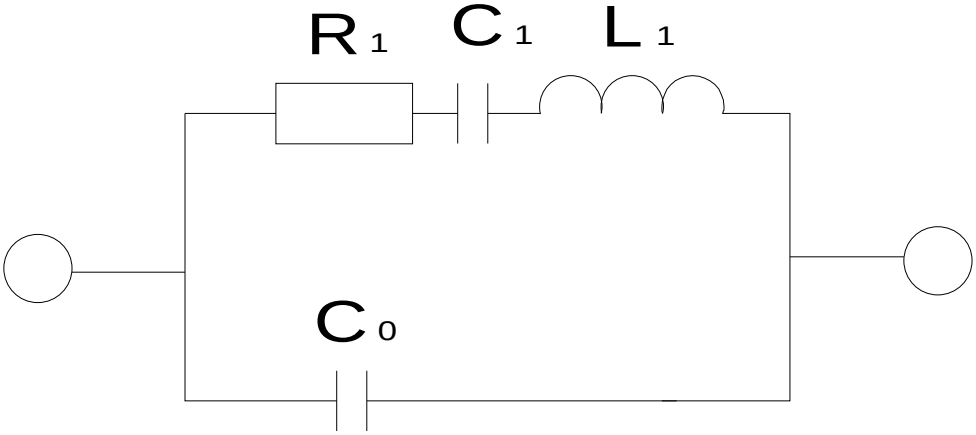

Fig. 6. Butterworth-van-Dyke equivalent circuit for the bare crystal

When applying a load to the QCM, we need to add other elements to the equivalent circuit. These elements depend on the sample we use. The BvD circuit is linear model. This model can not be used in nonlinear systems. It is useful only for simple systems. We will use the BvD circuit to describe a mass loading in a further section.

3.4. The QCM as instrument in contact mechanic measurements

In the previous section we have mentioned, that in order to derive the frequency shift we need to describe the quartz–sample interface. Discrete objects like spheres or sand are non a planar sample and the standard model of the planar systems can not be used. The modeling starts that from the assumption that the stress–speed ration may be replaced by an average stress–speed ratio, where the average stress is the lateral force divided by the active area of the crystal [55].

Once we have accepted this simple approximation, the frequency shift can be easily understood on the basis of the BvD equivalent circuit. Depending on the situation, spheres in

contact with the quartz crystal can be represented with a mass, a spring, a dash pot or with a combination of these elements. More information about the sphere–plate contact are given in reference [55]. There we are only interested in heavy objects in contact with the crystal. Such systems can be described with the Dybwad model [57]. This is the model of a spring in parallel with dashpot attached to a solid wall. The heavy mass behaves like a solid wall in this model. One more model will be used to describe the sphere–plate contact. This is the Mindlin model of partial slip. Actually, this is a nonlinear model and cannot be described in terms of BvD circuit. It is impossible to describe nonlinear behavior with such simple elements like the spring, the dash pot or the mass.

3.5. Dybwad model

In the following, we describe one sphere on the surface under tangential load. We mostly consider the surface of a quartz crystal under high frequency oscillatory shear. For small amplitudes, we shall consider either no "slip" or "partial slip". The sphere and the crystal stay in contact. Due to the oscillation of the crystal we have an oscillation for the center of mass of the sphere. Dybwad modeled the sphere–plate contact as a discrete point mass, coupled to the surface via a spring and a dashpot. This certainly is an approximation. Most of the sphere remains undeformed. The deformation is highly localized at the region of contact. The system of single sphere on the surface can be represented with the point mass, *m*, coupled to the crystal through a spring in parallel with a dash pot. The spring with the spring constant, κ, represents an elastic force and the dash pot with the drag coefficient, ξ, describes a withdrawal of energy from the oscillation (Fig. 7). The displacement of the crystal surface is described by the equation

$$u = U\exp(i\omega t) \qquad \text{Eq. 3.4}$$

The equation of motion for the mass–spring–dashpot assembly is [65]

$$m\frac{d^2w}{dt^2} = -\kappa(w-u) - \xi\frac{d}{dt}(w-u), \qquad \text{Eq. 3.5}$$

where $w = W\exp(i\omega t)$ is the displacement of the sphere. Here we understand displacement of the center mass, not slip of the sphere on the surface. $\omega \neq 0$ does not imply slip. During the oscillation sphere–plate contact stick.

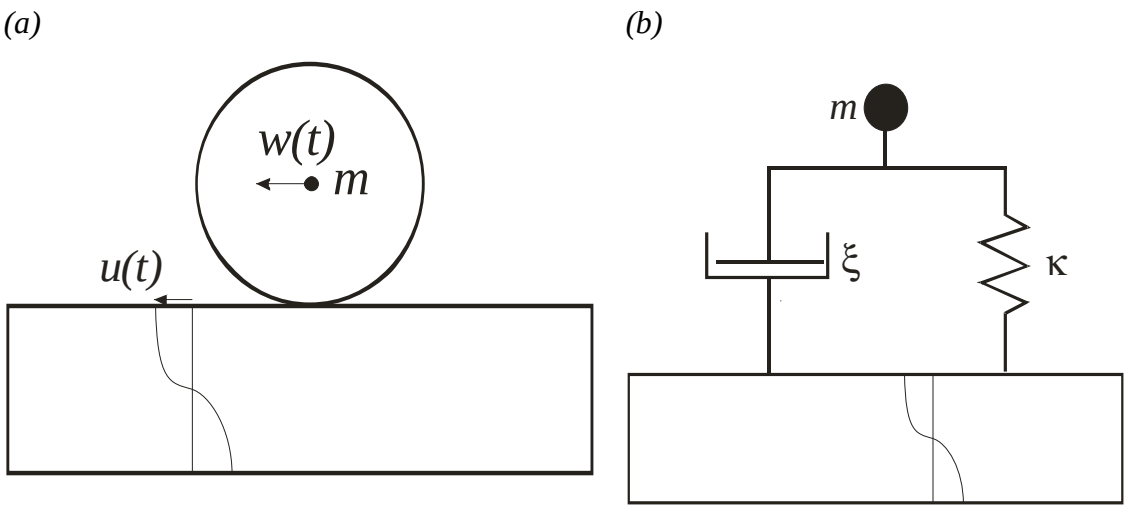

Fig. 7. Sphere–plate contact under tangential load (a) and modelling of this system (b)

We redefine the combination of parameters (κ/m) as the square of resonance frequency ω_s^2 and (ξ/m) as the damping coefficient of our system, γ. The stress exerted by the sphere onto the crystal is proportional to the relative displacement [65] and the exerted stress is

$$\sigma = -N\left(\kappa + i\omega\xi\right)\left(W - U\right) = Nm\left(\omega_s^2 + i\omega\gamma\right)\frac{\omega^2}{\omega^2 - \omega_s^2 - i\omega\gamma}U \qquad \text{Eq. 3.6}$$

where N is the number of the spheres per unit area. According to the small-load approximation [66], the complex frequency shift is

$$\frac{\Delta f + i\Delta\Gamma}{f} = \frac{i}{\pi Z_q}\frac{\sigma}{i\omega U} = \frac{Nm\omega}{\pi Z_q}\frac{\omega_s^2 + i\omega\gamma}{\omega^2 - \omega_s^2 - i\omega\gamma} \qquad \text{Eq. 3.7}$$

where f is the fundamental frequency of the quartz resonator, Γ is the half band half width (HBHW) of the resonance peak, and Z_q is the acoustic impedance of AT-cut quartz.

For ω much smaller than ω_s, the motion of the sphere is in phase with the motion of the crystal. In this case, the shift of the frequency is described by $\Delta f/f \approx -N\omega m/(\pi Z_q)$, which is equivalent to the Sauerbrey equation.

For the opposite limit, when we have the frequency ω_s much smaller than ω, we find [57, 58, 59, 60]

$$\frac{\Delta f + i\Delta\Gamma}{f} \approx \frac{N}{\pi Z_q \omega}\left(\kappa + i\omega\xi\right) \qquad \text{Eq. 3.8}$$

For $\omega_s << \omega$, the mass is too large to move with the crystal. The center of the mass nearly stays in place and does not take part in the oscillation. Frequency shift and HBHW are proportional to the spring and drag coefficient, respectively. Equation Eq. 3.8 predicts a positive frequency shift and a positive shift of the bandwidth.

3.6. Mindlin theory

The problem of a contact between a sphere and a plate under tangential oscillating force was first studied by Mindlin in 1952. The normal force remains constant. As in the Hertz theory, contact radius and pressure remain constant, as well. Application of a lateral force will cause micro-slip at the rim of the contact area. As a consequence, there is an annulus, inside which the two surfaces slide against each other. Inside the inner border of the slip region the contact of the two surfaces behaves elastically.

The Hertzian contact is nonlinear under tangential load. The consequences of a nonlinear interaction can be quantitatively predicted, as long as the nonlinearities are small. The influence of the sample onto the crystal must be small in order for the small-load approximation to apply. In QCM experiments, the frequency shift is always much smaller than the fundamental. A smaller frequency shift implies a smaller external load. This makes it possible to use the two-timing approximation for the analysis of QCM data. For a nonlinear oscillator, we can write the equation of motion in the form

$$\frac{d^2u}{dt^2} + u + \varepsilon h(T) = 0 \qquad \text{Eq. 3.9}$$

where $T=\varepsilon t$ is a second time, called "slow" time. ε is a small dimensionless parameter. The function $\varepsilon h(T)$ is a small perturbation of the oscillator. The perturbation depends on displacement and velocity of the movement. However, the algebra is unchanged if we write the perturbation as a periodic function with the period of the oscillation itself. The two-timing approximation starts from the ansatz [56]

$$u(t) = A(T)\cos\left(\omega_0 t + \Phi(T)\right) \qquad \text{Eq. 3.10}$$

The lateral displacement of the crystal $u(t)$ is almost harmonic with time . The consequences of the external force are captured by a slowly varying amplitude, $A(T)$, and phase, $\Phi(T)$, with time. In Eq. 3.10, ω_0 is the resonance frequency of the crystal itself. The

shift in the bandwidth is proportional to the "slow" time derivative of the amplitude and the frequency shift is proportional to the "slow" time derivative of the phase. Using perturbation theory, one arrives at the following time–averaged equations [59, 61]

$$\Delta f = \frac{1}{2\pi}\frac{d\Phi(T)}{dT} = -\frac{1}{A(T)\pi^2 A_{eff} Z_q}\langle h(t)\cos(\omega_0 t)\rangle$$
$$\Delta\Gamma = -\frac{1}{2\pi A(T)}\frac{dA(T)}{dT} = -\frac{1}{A(T)\pi^2 A_{eff} Z_q}\langle h(t)\sin(\omega_0 t)\rangle \qquad \text{Eq. 3.11}$$

The angular brackets denote that the average over an entire period of oscillation. We shall consider an oscillating tangential force of amplitude $\pm F$ applied to our sphere in contact. The first application of normal force in a positive direction will cause micro-slip in the rim $c \le r \le a$ of the sphere plate contact. a is the Hertz radius of contact. The parameter c is given by [67]

$$\frac{c}{a} = \left(1 - \frac{F}{\mu_s P}\right)^{1/3} \qquad \text{Eq. 3.12}$$

with μ_s the static friction coefficient and P normal force. The tangential displacement, $u(t)$, during unloading is given by [67]

$$u(t) = \frac{3\mu_S P}{8aG_{eff}}\left[2\left(1-\frac{F-F(t)}{2\mu_S P}\right)^{\frac{2}{3}} - \left(1-\frac{F}{\mu_S P}\right)^{\frac{2}{3}} - 1\right]$$
$$= \frac{3}{2}\lambda_S\left[2\left(1-\frac{F-F(t)}{2\mu_S P}\right)^{\frac{2}{3}} - \left(1-\frac{F}{\mu_S P}\right)^{\frac{2}{3}} - 1\right] \qquad \text{Eq. 3.13}$$

where $G_{eff}=2((2-\nu_1)/G_1+(2-\nu_2)/G_2))^{-1}$ is an effective modulus. G and ν are the shear modulus and Poisson ratio, respectively. When the tangential force is completely reversed, ($F = -F$ in equation Eq. 3.13) the relative displacement changes sign. The characteristic length $\lambda_s=\mu_s P/(4aG_{\text{eff}})$, is defined in analogy to the elastic length used by Paris group to describe multiasperity contacts. The elastic length is $\lambda=P/\kappa$ [70, 71, 72]. The tangential displacement of the sphere relative to the surface as given by Eq. 3.13 shown in Fig. 8.

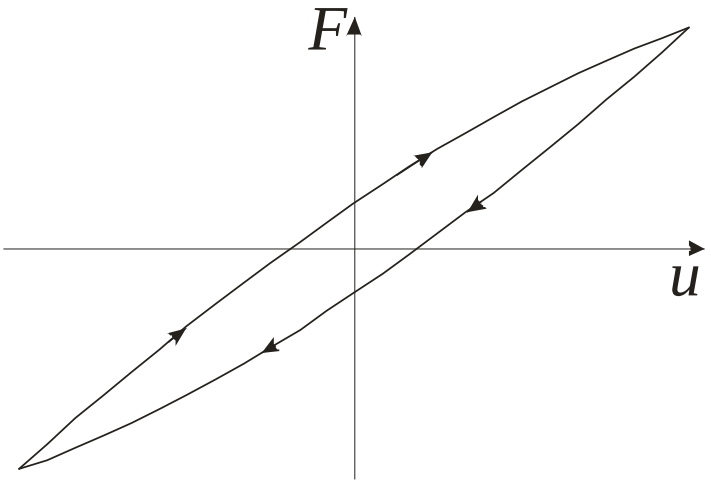

Fig. 8. Load–displacement cycle of the sphere–plate contact under oscillating tangential load.

The energy dissipation per cycle is the area inside the hysteretic loop. This energy does not depend on the frequency. However, it does depend on the amplitude of motion.

Since we are working in small load regime, the force in the contact area only weakly perturbs the motion of the quartz crystal surface. The displacement, $u(t)$, is sinusoidal with time and mainly governed by the dynamics of the crystal. The lateral force, $F(t)$, can be calculated by inversion of Eq. 3.13 and we obtain:

$$\frac{F(t)}{\mu_S P} = \left[\frac{F}{\mu_S P} - 2 + \frac{1}{\sqrt{2}} \left(1 + \frac{2u(t)}{3\lambda_S} + \left(1 - \frac{F}{\mu_S P} \right)^{\frac{2}{3}} \right)^{\frac{3}{2}} \right] \qquad \text{Eq. 3.14}$$

Substituting Eq. 3.14 into Eq. 3.11 and performing the integration, we find frequency shift, Δf, and HBHW, $\Delta\Gamma$, as a function of the amplitude of motion:

$$\frac{\Delta f}{f_f} \approx \frac{1}{A_{eff} Z_q \pi} \frac{4aG_{eff}}{\omega} \left(1 - \frac{1}{6} \frac{A}{\lambda_S} \right) = \frac{1}{A_{eff} Z_q \pi} \frac{\kappa_{0,M}}{\omega} \left(1 - \frac{1}{6} \frac{A}{\lambda_S} \right) \qquad \text{Eq. 3.15}$$

$$\frac{\Delta\Gamma}{f_f} \approx \Delta\Gamma_{sound} + \frac{1}{A_{eff} Z_q \pi} \frac{\kappa_{0,M}}{\omega} \frac{2}{9\pi} \frac{A}{\lambda_S} \qquad \text{Eq. 3.16}$$

To perform the analytical integration, we have use the small amplitude limit ($u(t) << \lambda_s$). The details of these calculations can be found in reference [73].

Value of $4aG_{\text{eff}}$ can be defined as the spring constant in the small amplitude limit $\kappa_{0,M}$. $\kappa_{0,M}$ is experimentally available via the frequency shift, Δf. Making assumption on G_{eff}, one

calculates a contact radius based on this relation. This radius is termed “Mindlin radius”, $R_{Mindlin}$, in the results section (see, for example, Table 2 in section 4.34.6). $\Delta\Gamma_{sound}$ is the dissipation caused by radiation of the sound into the sphere. Frequency shift and bandwidth vary linear with the amplitude. The system can not be represented with discrete elements like a spring or a dashpot.

In the low amplitude limit the slope in the plot of Δf versus amplitude A is given by $f_f\kappa_{0,M}/(6A_{eff}Z_q\pi\omega\lambda_s)$. λ_s, in turn, is given by $\mu_s P/(4aG_{eff})$. Science all parameters other than μ_s are known, one can calculate the static friction coefficient, μ_s, from the plot of Δf vs A (see, for example, Table 2 in section 4.7).

As Bowden and Tabor have emphasized, an understanding of friction phenomena must include the microscopic scale [77]. Since the contact is usually made across small asperities, the true contact area is much smaller than the apparent contact area. What appears as steady sliding, macroscopically, may be a succession of sticking and detachment events on the local scale. Following Boden and Tabor, one expresses the friction force $F_{\|}$ as $F_{\|} = \sigma_{\|}\,\Sigma_r$, where $\sigma_{\|}$ is a critical stress and Σ_r is the real area of contact. In particular, the static friction coefficient describing the onset of sliding is higher than the dynamic friction coefficient.

The static friction coefficient as derived with the Mindlin model is $\mu_s=\lambda_s\, 4\, a\, G_{eff} / F_{normal}$, where a is radius of the contact and proportional to the frequency shift, Δf_0. λ_s does not depend from the amplitude. It is calculated from the linear fit to the experimental data. Obviously, it depends on the slope of the frequency shift curve (see, for example, Fig. 10). Hence, the static friction coefficient depends on the square root on the area of contact, not on the area itself. Therefore, this is in discrepancy with the model of Bowden and Tabor.

4. Contact mechanics measurements via the drive level dependence of Δf and $\Delta\Gamma$

4.1. Introduction

Contact mechanics has been studied for a long time. Understanding and controlling friction and adhesion between the solids has been a topic of research for hundreds of years. In the last years we have seen a great development in nano techniques. On the nanoscale or the atomic scale, physical properties have a different character in the bulk.

This study is primary motivated by the interest in the fundamentals of friction and it dependence on humidity. We study sphere plate contacts under high frequency oscillatory shear. Small spheres were placed onto the front electrode of a quartz crystal resonator. The Mindlin model of partial slip is in a good agreement with the results which we find in drive level experiments. In this model the transition from static friction to sliding is continuous. Application of a tangential oscillatory force, induces a stress concentration at the rim of the contact area. As a consequence, there is the area at the rim of contact, in which two surfaces slide against each other. This phenomenon is called “partial slip”.

In this part of the work we compare the experimental results, analyzed in the framework of Mindlin model, with the Hertz model of elastic contact between sphere and plate. The Mindlin model predicts real area of the sphere plate contact from the experimental data. From our results section the real area is always smaller than what one calculates from the Hertz theory. In the results we the describe influence of the high frequency oscillatory motion onto the strength of the sphere–plate contact.

As a new effect, we describe the strengthening of the contact after dry–humid–dry cycle. This effect is termed sandcastle effect. In the sandcastle effect, menisci form in the contact area in high humidity. Finally, with the drying of the liquid, capillary forces elastically deform the surfaces. The area of the contact becomes much larger it was initially. The sandcastle effect was observed for the different environments.

4.2. Experimental details

The experiments were performed with AT-cut quartz crystals with a size of 1 inch and a fundamental frequency of 5 MHz (Maxtek Inc., Santa Fe Springs, CA). The crystals were coated with gold electrodes and mounted in a home-built holder. Frequency and bandwidth were determined by impedance analysis with an accuracy in the determination of the resonance frequency below 1 Hz. The coupling between mechanical displacement and electrical potential in the piezoelectric quartz makes it possible to measure the current through the electrodes (that is, the conductance) instead of measuring mechanical oscillations. It is convenient to use an equivalent circuit model to describe the electrical behavior of the QCM. In our experiments, a network analyser (HP E5100A, HEWLETT PACKARD) sweeps the frequency across the resonance and determines the admittance, $Y(\omega)$. With impedance analysis, both frequency and bandwidth were determined for the different overtones. Usually, no more than two overtones were used. All experiments were conducted at room temperature without temperature control.

The drive level dependence (DLD) measurements were performed in the range of drive power from –55 dBm to the +22 dBm (where 0 dBm corresponds to a power of 1mW). The conversion between electrical power in units of dBm to the driving voltage across the electrodes is $U_{el}=0.317\ 10^{(power[dBm]/20)}$ [40]. The relation between the amplitude, A, of oscillation and driving voltage is given by

$$A=\frac{4}{(\pi n)^2}d_{26}QU_{el} \qquad \text{Eq. 4.1}$$

where n is the overtone order, d_{26} is the piezoelectric coefficient, and Q is the quality factor (Eq. 3.3). To control the humidity, the quartz crystal was placed inside a plastic box. The humidity was measured with a portable humidity temperature sensor (Rotronic A1H, HYGROMETER). To increase the humidity inside the plastic box, we used wet filter paper soaked in water. A fan was used to induce convection. A powder of phosphorous pentoxide (P_2O_5) was used to induce dry conditions inside the plastic box.

As samples for the DLD measurements we used glass spheres. The spheres used in the experiments had four different ranges of diameter (100–112μm, 193–225 μm, and 674–746 μm). The spheres were mounted to a metal substrate with the double sided tape (see Fig. 9). The soft backing ensures that all spheres come into contact with the crystal, when this assembly is placed onto the crystal. The number of spheres depends on their size. For the

biggest one we have used fewer spheres than for the smaller glass spheres. The mass of such a system is about 1g.

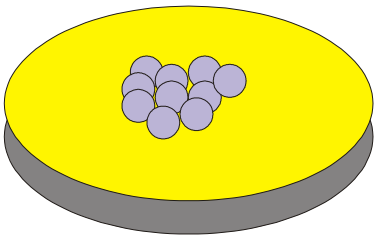

Fig. 9. Schematic image of the sample with the spheres.

To understand the behavior of the assembly of the spheres, we have performed a series of experiments with a single Si_3N_4 sphere. We have used spheres with a size of 4.76 mm and 6 mm.

In our experiments we have made drive level measurements in a dry–humid–dry cycle. Dry–humid–dry cycle means that we have three stage of our experiment:

- Three or four drive level measurements in dry conditions. The humidity inside the plastic box with quartz crystal and sample is lower that 15 %rH. These experiments are performed with increasing maximal drive level.
- Two or three experiments under high humidity conditions (> 70 %rH). These two or three experiments are performed with the different maximum drive levels and, as a consequence, different maximum amplitudes.
- Drying the plastic box with quartz crystal and sample. The humidity is lower than 30 %rH. Several experiments with the different maximum amplitude are performed.

The most interesting effect takes place during drying of the sphere–plate contact. For this reason we have made several experiments, where we have placed a liquid droplet on the top of quartz crystal surface. Afterwards we immersed the sample into this droplet. In this way, the sphere–plate contact is totally wet. Drive level measurements were performed from wet conditions until the sphere–plate contact was totally dry.

In our experiments we have used water and organic liquids such as acetone and ethanol to create a wet sphere–plate contact.

4.3. Single sphere contact

In order to better understand the mechanism of partial slip and the sandcastle effect, we have performed a series of measurements with a single Si_3N_4 sphere. We have used spheres with a diameter of 4.76 mm and 6 mm. For reasons of cleanliness, thermal stability, and control of humidity, the setup was enclosed in a plastic box.

Before the start of the measurement, we determined the reference state for the bare crystal at a drive level 0 dBm. The relative humidity inside the box was about 9%.

Then we placed a single sphere on the top of crystal surface and waited for 12 hours, before we started the measurements. The reason for this was to exclude a time dependence of contact strengthening. Fig. 10*a* and *b* show the result. These two measurements differ in the maximum drive level. In the experiments shown in Fig. 10*a* we have used a maximum drive level of –10 dBm. This drive level corresponds to the maximum amplitude about 5 nm. With this amplitude, there is no increase in frequency shift, Δf_0, during the drive level cycle. In the case of a maximal drive level of 20 dBm, we reach an amplitude of shear motion of more than 200 nm. After the first cycle, the frequency shift, Δf_0, increases from 100 Hz to 225 Hz. The results are shown Fig. 10*b*. The arrow labels the direction of the drive level sweep. An increase in the frequency shift, Δf_0, corresponds to an increase of the Mindlin radius of contact and, as a consequence, an increase of strength of the sphere–plate contact. This strengthening is caused by the high-amplitude shear motion. In the following we will call this effect *shear-induced strengthening* of the contact.

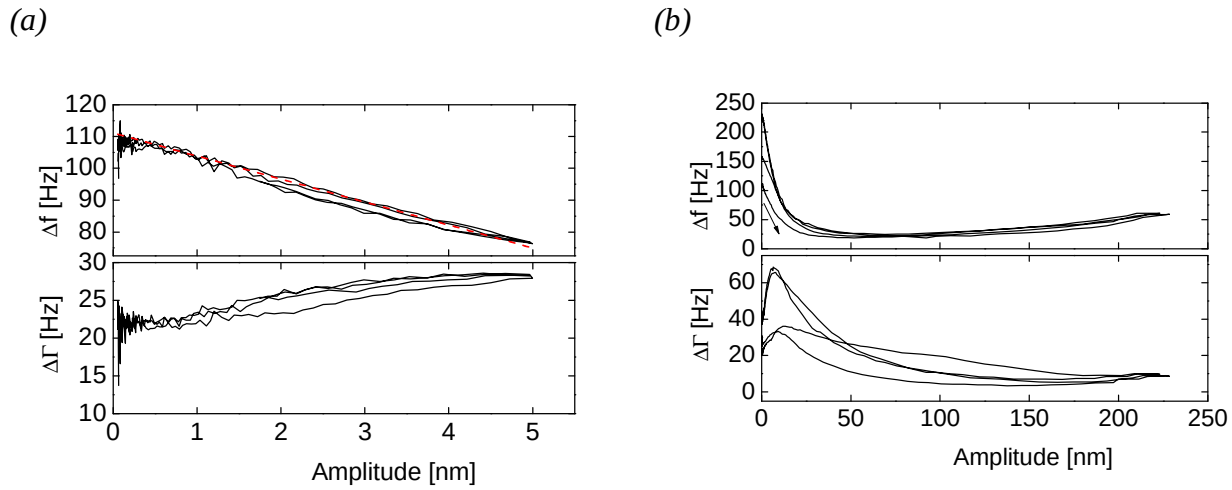

Fig. 10. Results for the measurement on a single Si_3N_4 sphere with a diameter of 4.76 mm and a mass of 0.178 g. (a) rH=9%, drive level range from –50 dBm to –10 dBm. The dashed line is linear fit. (b) rH=9% drive level range from –50 dBm to 20 dBm

A further experiment was performed in a humid environment. We have increased relative humidity inside the plastic box up to 80 %rH. A humid atmosphere produces liquid menisci and water bridges at the points of contact. We have waited for 5 hours to achieve stable conditions, before the started the measurement, because the creation of menisci takes time. The result of this measurement is shown in Fig. 11*a*. The start of the measurement is labeled with an arrow. At the beginning, the frequency shift, Δf_0, is higher than after subjecting the sample to high shear. The reason for increase in the frequency relative to the dry state (Fig. 10) is a strengthening of contact due to the capillary forces. After the first cycle frequency shift, Δf_0, decreased from 330 Hz to 255 Hz. This decrease of the frequency is caused by the high shear amplitude. In this experiment we have used a maximum drive level of 20 dBm. This corresponds to an amplitude of more than 200 nm. The high shear amplitude destroys water bridges and makes the sphere–plate contact weaker. A decrease of the frequency shift, Δf_0, and as consequence, weakening of the strength of the contact caused with shear amplitude will be call *shear–induced weakening* in the following.

In the next stage of our experiment, we decreased the relative humidity. During the experiment, the relative humidity inside the box was lower than 25 %rH. After drying of the contacts we have used a maximum drive level of 10 dBm. Decreasing of humidity and drying the sphere–plate contact leads to an increase of the frequency shift and the bandwidth. These changes in frequency and in bandwidth are much large than what we have observed in shear–induced strengthening and with increasing of humidity. The quality factor, Q, in Eq. 4.1 is inversely proportional to the bandwidth. Therefore, the significant increase in bandwidth

decreases the amplitude for equal drive level before and after drying of the contact. The drive level of 10 dBm after drying corresponds to an amplitude of about 20 nm.

The large increase in frequency shift, Δf_0, is explained as a result of the sandcastle effect. Upon drying, the radii of curvature of all menisci decrease. As a consequence, the Laplace (Eq. 2.11) pressure increases and elastically deforms these regions into having a greater contact area. More information about the sandcastle effect and the processes which take place during dry–humid–dry cycle are given in section 4.12.

In the experiments with a drive level of 10 dBm, we observe partial destroying of the sandcastle effect. During the experiment we have a weakening of the sphere–plate contact. Fig. 11*b* shows frequency and bandwidth versus time. In all of the drive level cycles, the frequency shift, Δf_0, becomes smaller.

Further increasing the drive level or the amplitude (what is the same) would completely remove of the sandcastle effect. Total removal of the sandcastle effect is very fast process. When the drive level and the amplitude are high enough to destroy the sandcastle, the contact are disrupted. In parallel the bandwidth decreases. Decrease of the bandwidth leads to an increase amplitude. The increase in amplitude leads to an even faster removal of the contacts. The process therefore is self-accelerating. This is like an avalanche of amplitude. After removing of the sandcastle effect, we have a Δf_0 value of 175 Hz. This value for the frequency shift is similar to the frequency shift that we had before the dry–humid–dry cycle.

(a) *(b)*

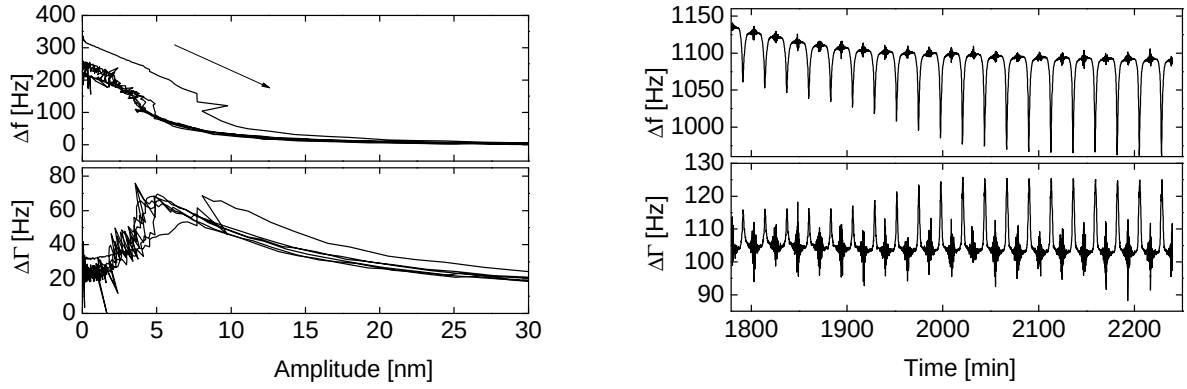

Fig. 11. Results for the measurement on a single Si_3N_4 sphere with a diameter of 4.76 mm and a mass of 0.178 g. (a) rH=80%, drive level range from –50 dBm to 20 dBm. (b) rH=25%, drive level range from –50 dBm to 10 dBm.

A summary of the quantitative analysis of these results is shown in Table 1. In this table we can see experimental data and data from the calculations based on the Hertz theory of elastic contact and on the Mindlin theory of elastic contact under tangential shear force. For the calculation we have used values 310 GPa and 72 GPa for the Young modules, 0.27 and 0.23 for the Poisson ration for the Si_3N_4 and the quartz surface respectively. We have neglected the gold electrode since it is much thinner than the contact radius.

The "Hertz radius" of the elastic sphere–plate contact, R_{Hertz}, was calculated from Eq. 2.2. In the Mindlin theory, the frequency shift, Δf, is a linear function of amplitude (Eq. 3.15). In our results, we often have a plateau at very small amplitudes and a linear decrease at somewhat higher amplitudes. The plateau at the lowest amplitudes will be discussed later in this chapter. Here, we are interested the region of amplitudes where we have linear decrease of the frequency with increasing amplitude. This behavior is predicted by the Mindlin theory.

Applying a linear fit to the experimental results in the small amplitude range, we find two parameters of linear function. A typical linear fit is shown in Fig. 10*a*. The Mindlin theory is only correct in the small amplitude limit. Comparing the coefficient from the fit function with theEq. 3.15, we find a spring constant, $\kappa_{0,M}$, and characteristic length, λ_s. λ_s was defined as $\mu_s P/\kappa_{0,M}$. From the value of λ_s we can derive the static friction coefficient μ_s. $\kappa_{0,M}$ was defined as $4aG_{eff}$ where a is the radius of the contact. We will call this radius of contact (calculated from Mindlin theory) Mindlin radius of the sphere–plate contact, $R_{Mindlin}$.

Table 1. Table of results for the single Si_3N_4 sphere. The diameter of the sphere is 4.76 mm. The mass is about 0.178g.

No	rH[%]	Δf_0[Hz]	$\Delta\Gamma$[Hz]	R_{Hertz}[μm]	$R_{Mindlin}$[μm]	λ_s[nm]	κ[kg/s^2]	μ_s
1	09	111	21	3.7	5.7	2.5	$0.74\,10^6$	1.06
2	09	160	26	3.7	10.0	3.6	$1.06\,10^6$	2.2
3	80	332	21	3.7	20.7	2.5	$2.22\,10^6$	3.17
4	25	1132	103	3.7	70.5	59	$7.56\,10^6$	255
5	25	1098	103	3.7	68.5	34	$7.32\,10^6$	142

The first line contains the results for the sphere–plate contact in the initial state. We have strengthening of the contact with amplitude or with humidity. The second line contains

the results obtained after shear-induced strengthening. In the third line we show the obtained results after increasing the humidity in the box. In the next part of our experiment, we have a dry box (humidity decreased to 25 %rH). With drying of the sphere–plate contact, the sandcastle effect takes place. In the table, we see a large increase in frequency shift, Δf_0. This result is shown find in the fourth line. Then, we have tried to destroy the sandcastle effect by high amplitude oscillations. Partial destroying or weakening of the sandcastle effect occurs at an amplitude of about 20 nm. The results of our experiments after we have partial weakening of the sphere–plate contact are shown in the fifth line of the Table 1.

From Table 1 we see that the Mindlin radius is larger than the Hertz radius of elastic contact. We will see later for the glass spheres that the Mindlin radius before strengthening is smaller than the Hertz radius. An increase of the Mindlin radius is in good agreement with the theory of the sandcastle effect. This in more details discussed in section 4.12, where we in describe the processes that take place in all stages of the experiment.

The static friction coefficient, μ_s, after drying of the contact increases by two orders of magnitude. This value is much higher than predicted by the other experiment and theories. In these results, the high frequency of our experimental setup also plays a significant role. After weakening of the contact, the Mindlin radius of contact decrease to a small value. The static friction coefficient also decreases by a factor of 2.

In the previous discussion, we have dealt with those parts of the results, where we have a linear decrease of the frequency shift, Δf, with increasing of the shear amplitude. This part is in good agreement with the Mindlin theory. The decrease is a consequence of partial slip.

Interestingly, we sometimes observe plateau at the smallest amplitudes (amplitudes smaller than 5 nm). There is no dependence of the frequency shift, Δf_0, on amplitude. This plateau means that we are in the point contact regime where no partial slip occurs in the sphere – plate contact.

In the following, we examine the experimental results in the amplitude range smaller that 5 nm. In this range of amplitudes, we observe a plateau. At these amplitudes there is no partial slip. Frequency shift and bandwidth are independent from amplitude. Frequency shift and bandwidth shift in this case are described by Eq. 3.8.

Fig. 10*a* shows the drive level dependence in low humidity before shear-induced strengthening. We observe a plateau at amplitudes smaller than 0.25 nm. Fig. 11*a* is zoom into Fig. 10*b*. This is the results after shear-induced strengthening of the sphere–plate contact. In this result, we observe a plateau up to an amplitude of 1 nm. Compared to the result before

strengthening, the plateau has increased. With increasing contact strength, the plateau becomes wider.

(a) *(b)*

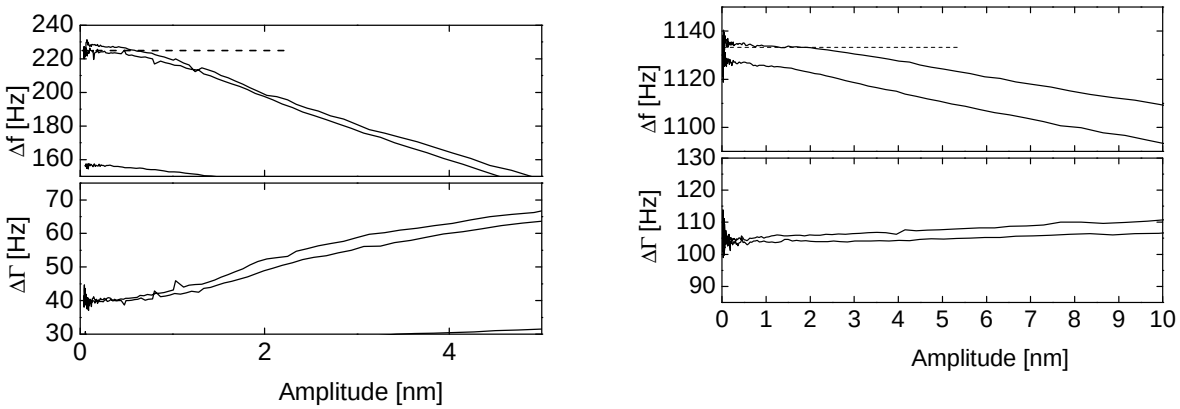

Fig. 12. Results for the measurement of a single Si_3N_4 sphere with the diameter of 4.76 mm, mass 0.178 g. (a) Relative humidity inside the plastic box is 9 %rH. Measurement performed after strengthening of contact induced with amplitude. (b) Relative humidity inside the plastic box is 9 %rH. Measurement performed after dry–humid–dry cycle.

Further experiment in our series occurred at high humidity. Here, the strength of the sphere–plate contact increases due to capillary forces. In these results, we have a plateau up to an amplitude of 2 nm. The width of the plateau is increased, compared to the previous results. The next stage is the drying of the contact. Upon drying of the contact we have a larger increase of the strength of contact (sandcastle effect). In sandcastle results, the width of the plateau is about 2.5 nm.

There is clear correlation between the contact strength and the width of the plateau.

4.4. Single sphere in water droplet

In the previous experiments on the Si_3N_4 sphere, we observed interesting changes of sphere–plate contacts after dry–humid–dry cycles. At high humidity, we observed an increase of the stiffness of the sphere–plate contact. This effect is based on capillary forces arising from vapor condensing around the contacts. During drying, capillary forces elastically deform the surface into having a bigger area of contact. High humidity causes a partial wetting of the contact area. What happens if we have a fully wet contact? To answer this

question, we performed a series of experiments, where we placed a droplet of liquid on top of the quartz crystal and placed the sphere into this droplet. In this way, all free space between the sphere and the crystal surface is filled with water. The whole area of contact takes part in creating the sandcastle effect.

At the start of the measurement, we acquired the reference state with a bare quartz crystal. Then, we placed a water droplet on the crystal and placed the single Si_3N_4 sphere into the droplet. As expected, we obtained a negative frequency shift, caused by the presence of the liquid (Fig. 13*a*).

(a) *(b)*

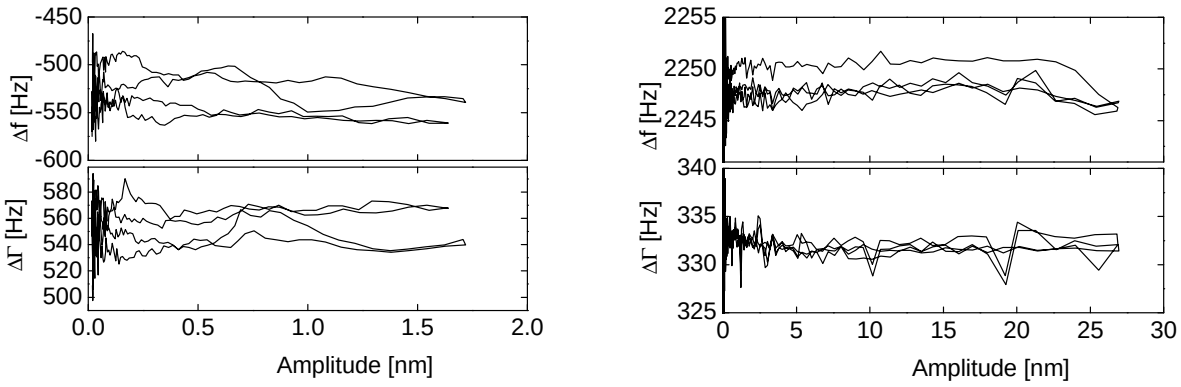

Fig. 13. Results of the measurement on a single Si_3N_4 sphere with a diameter of 4.76 mm and a mass of 0.178 g. (a) Results acquired in the presence of the water droplet. (b) After drying all the water. Drive levels from –40 dBm to 20 dBm.

Upon drying, the frequency shift becomes positive. After the end of drying, we have a large shift in frequency, Δf_0, and in bandwidth, $\Delta\Gamma$, (Fig. 13*b*). A high increase of the bandwidth makes it impossible to reach a high amplitude of motion even at the highest drive level. A maximum drive level of 20 dBm corresponds to a shear amplitude of 20 nm. From this result, we see that there is no dependence of the frequency on the shear amplitude. The contact between sphere and plate is very strong. There is no partial slip occurring even at a shear amplitude of 20 nm. The sphere and the crystal surface accomplish a shear movement like a bulk object.

In the following, we will compare the results for the humid and totally wet contact. The frequency shift, Δf_0, after drying of the totally wet contact is two times larger than what we have after dry–humid–dry cycles. As a consequence, the Mindlin radius of contact is also two times larger. The coated area is four times larger. The sandcastle produced with the

totally wet contact is much stronger than what we have for the dry–humid–dry experiment. For the measurements with variation of humidity, it was possible to destroy or at least weaken the sandcastle by shear. In contrast, in the later result, the sphere–plate contact stayed stable even with the highest drive level of 20 dBm.

When comparing the results obtained with a droplet of bulk water with dry–humid–dry cycles, we see that in the case of the water droplet the sandcastle effect is stronger. This is explained by the fact that in the water droplet we have totally wet contact. During drying all the area of contact takes part in sandcastle effect. For a humid atmosphere, the sandcastle is only created via asperities where we have liquid menisci.

4.5. Sandcastle effect in single sphere–plate contact with organic vapors

In the previous chapters, we have discussed experiments with a single Si_3N_4 sphere. We have observed an increase of contact stiffness upon variation of humidity. The explanation for such an increase of contact stiffness is the capillary forces of the menisci and water bridges. In principle, strengthening of sphere–plate contacts could also be the result of salt bridges or contaminants accumulating at points of contact. To check for this salt-bridges hypothesis we can employ organic liquids. We used acetone and ethanol.

The entire sample was placed into a plastic box. We dried the environment inside the box to a relative humidity lower than 6 %rH. Before the start of the measurement we determined the reference state for the bare crystal at a drive level 0 dBm. The experiment was carried out in three stages.

First stage. We placed the sphere on the quartz crystal. After we place the sample on to the crystal, there is a relaxation process. Therefore, we have to wait for two hours in order to eliminate effect from relaxation processes.

For the experiments with ethanol and acetone we used two similar Si_3N_4 spheres. The result for the single sphere in dried box is shown in Fig. 14. This result was obtained with a small shear amplitude. There is no shear–induced strengthening in this figure. For the second sample in the dry state we have used maximum drive level. This amount of shear did induce strengthening of the sphere–plate contact. Further, we have used this sample in an acetone environment.

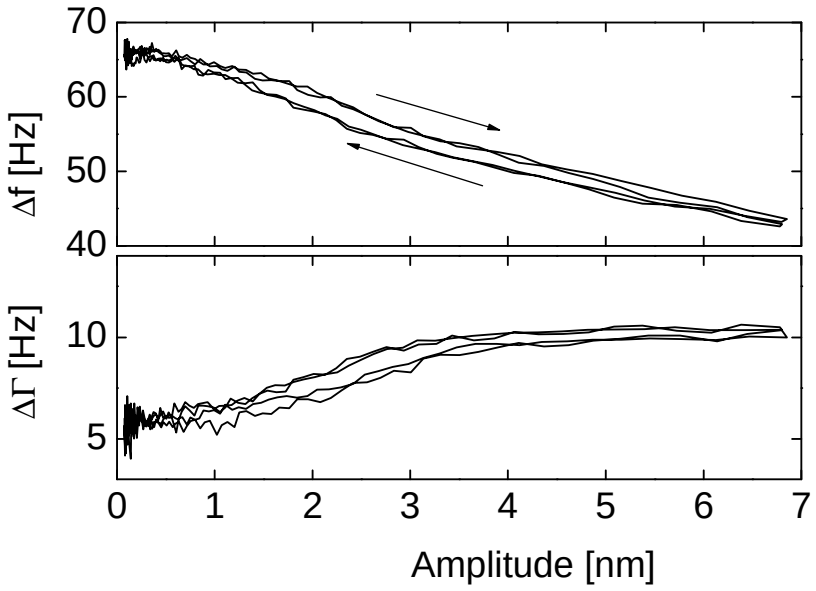

Fig. 14. Results of measurement on a single Si_3N_4 sphere (without acetone or ethanol). Drive level range: –50 dBm to –10 dBm. The relative humidity: 6 %rH.

Second stage. We have placed the first sample into the box containing ethanol and the second one into the box containing acetone. The drive level measurement was started immediately. We do not have any instrument to control vapor pressure of acetone or ethanol inside the plastic box.

Fig. 15*a* shows results obtained in acetone vapor. Acetone evaporates very fast. We see an increase in the frequency shift, Δf_0, during the first drive level cycle. The beginning of the measurement is labeled with an arrow. In ethanol, we find the opposite. We do not see any changes after the first two drive level cycles. We have waited for five hours and repeated the measurement with acetone and ethanol. For acetone there are no more changes in frequency and bandwidth. For the ethanol, we do observe an increase in the frequency shift, $\Delta f_{0,}$ (Fig. 15*b*). For both liquids there are no significant changes in HBHW.

The vapor pressure of acetone is about five times large than the one of ethanol and about ten times large than the one of water. That means that acetone evaporates in to environment much faster than ethanol or water. This explains why, we observe increasing in the frequency shift, Δf_0, after first drive level cycle. Ethanol needs more time to fill the camber with the vapor and to condense in the contact area.

Getting back to the results with the water vapor (Table 1) we see that frequency shift, Δf_0, for 9 and 80 %rH is larger than 100 Hz. For the organic liquids this difference is about 15 Hz. We can explain this by the weak capillary forces in comparison with the water. The

high vapor pressure of acetone and ethanol is the reason that we have a small number of menisci and liquid bridges in the area of contact.

The difference in the frequency shift, Δf_0, in Fig. 15 for the measurements in acetone and ethanol atmosphere is the reason of shear-induced strengthening. As we mentioned before, one of the sample was a subject of high shear. This sample we are using with an acetone. And for this sample we have higher frequency shift, Δf_0.

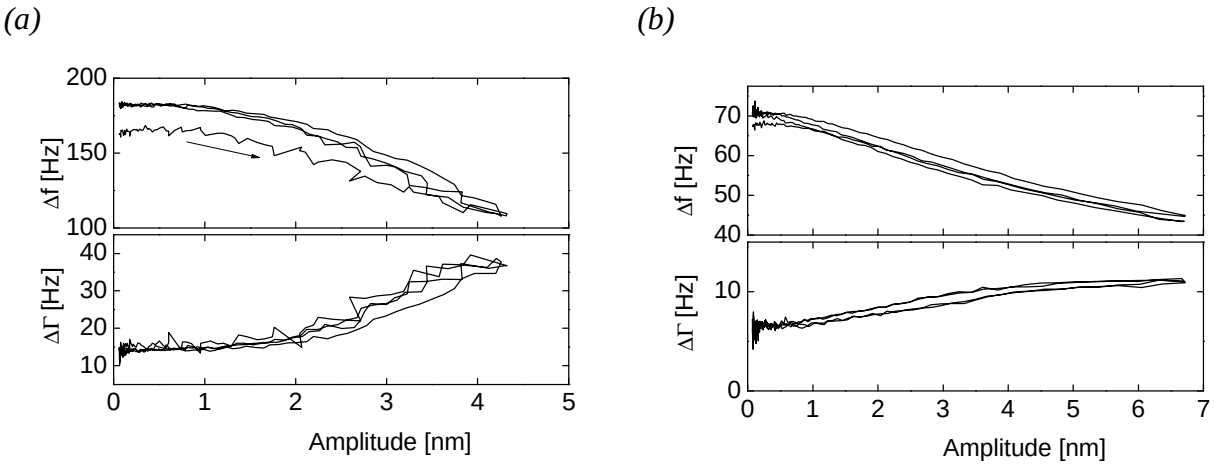

Fig. 15. Results of the measurement on the single Si_3N_4 sphere. Drive level from –50 dBm to –10 dBm. relative humidity is 6 %rH. (a) After we have placed a vessel with acetone inside the box. (b) Measurement five hours after we placed vessel with ethanol inside the plastic box .

Third stage. In this stage, we dried the plastic box from vapors of acetone or ethanol. With the drying of ethanol and acetone we expect to observe the sandcastle effect.

Fig. 16 shows the results after drying of the chamber. Fig. 16*a* corresponds to the sandcastle effect after a dry–humid–dry cycle in acetone environment. Fig. 16*b* shows the same data for ethanol. The sandcastle effect that takes place after dry–humid–dry cycle with organic environment. But it is weak. As discussed before, ethanol and acetone have smaller capillary forces in comparison with the water. High vapor pressure makes it possible only for a small amount of the asperities to take part in sandcastle effect.

Still, we have observed the sandcastle effect in our experiment. This makes us conclude that in the experiments with the water salt plays minor role.

(a) *(b)*

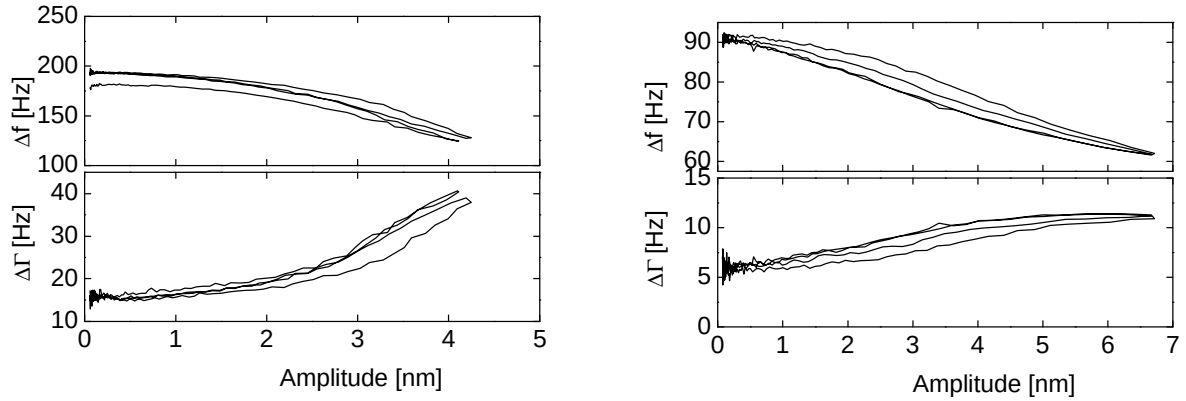

Fig. 16. Results for the measurements on a single Si_3N_4 sphere after drying of the box. The relative humidity inside the box is 15 %rH. Drive level range: –50 to –10 dBm. (a) Drying from acetone. (b) Drying from ethanol.

4.6. Sandcastle effect in single sphere–plate contact with organic liquid

In the measurements with the water we have observe a sandcastle effect for totally wet contact. In order to create a totally wet contact, we have placed the sample into a droplet of the water on the top of quartz crystal surface. The same was performed with organic solvents.

As before, we have started the experiments by determination of the reference state with a bare quartz crystal at 0 dBm. A droplet of acetone was placed on top of the quartz crystal. Into this droplet, we placed the single sphere and started the measurement. With acetone on the surface, we have a negative frequency shift and an increased HBHW, $\Delta\Gamma$, (see Fig. 17*a*). Acetone evaporates quite fast and during first cycle, most acetone is evaporated. With the evaporation of the acetone from the surface, the frequency shift goes to positive. After total evaporation of the acetone, the resulting frequency shift is about 470 Hz and the HBHW is in the range of 45 Hz.

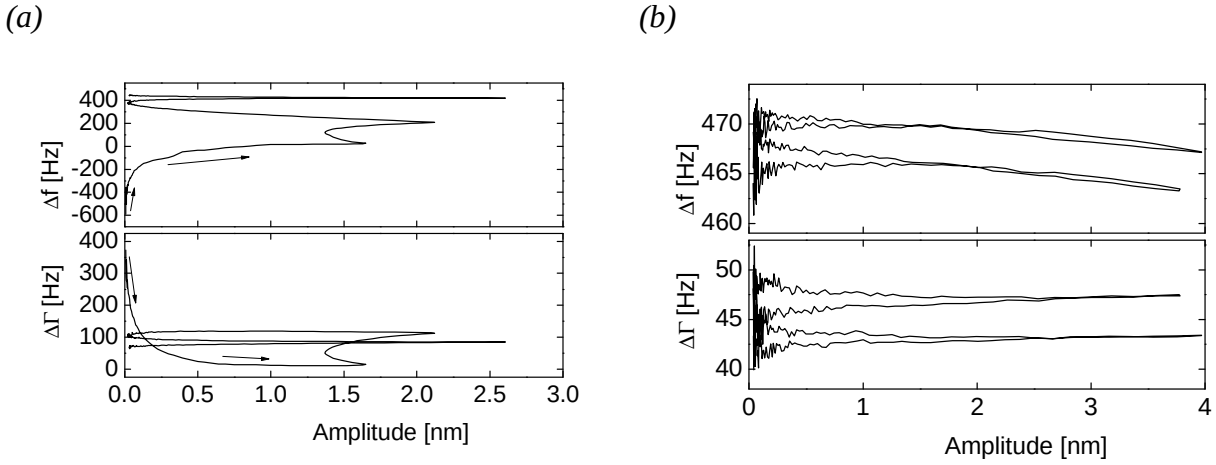

Fig. 17. Results for the measurements on a single Si3N4 sphere in acetone droplet. (a) Dduring evaporation of acetone droplet. (b) After all acetone has evaporated.

Comparing frequency shift, Δf_0, with the results from Fig. 14, we see an increasing in the frequency. The increase after drying of acetone describes the sandcastle effect. With a droplet of acetone, this effect is much stronger than for acetone and ethanol vapors. With a droplet of liquid, the sandcastle effect takes place at the whole area of the contact between sphere and quartz crystal surface. In the case of vapors, the vapor creates menisci at the points of contact only. The vapor pressure for the ethanol and acetone is higher than for the water. We have vapor condensation only for the small amounts of nanosized asperities. If the Kelvin radius exceeds the distance between two points not initially in contact, new liquid bridges arises between these two points. The Kelvin radius calculated with Eq. 2.10 is smaller for these organic solvents in comparison with water. This can explain the poor strengthening of contact after drying of acetone and ethanol.

4.7. Glass spheres with the diameter of 700 μm

The results obtained on a single sphere help to understand the “partial slip” and the sandcastle effect in contacts between a sphere and a plate. In this part, we discuss experiments with many glass spheres. The glass spheres have a much smaller size than the single Si_3N_4 sphere. A schematic image of the sample with the spheres is shown in Fig. 9. In this part of the work, we present results for glass spheres with a diameter of 700 μm. The number of the glass spheres we used for the sample preparation, is 20.

Before the start of the measurement we placed the QCM and the sample inside the plastic box and dried the box to a relative humidity lower than 9 %rH. After drying, we determined the reference state for a bare crystal at a drive level 0 dBm.

After having placed the sample on the quartz crystal surface, we waited for 12 hours before the start of first measurement. The reason for this was to exclude an influence of relaxation processes from experiment. The first measurement was performed with a maximal drive level of –10 dBm. The result for this measurement you is shown in Fig. 18*a*. There is no increase in the frequency shift, Δf_0, with the drive level cycles. The contacts between the spheres and quartz crystal stay stable at this shear amplitude. Also, the behavior is almost reversible with increasing and decreasing shear amplitude. The next measurement (Fig. 18*b*) was performed with a maximum drive level of 20 dBm. With a drive level of 20 dBm, we reach an amplitude of shear motion above 200 nm. With such a high amplitude of oscillations, we observe shear-induced strengthening of the contact between the spheres and the quartz crystal surface. In Fig. 18*b*, we observe an increase of the frequency shift, Δf_0, during the drive level cycles. The arrow shows the direction of the first drive level sweep. At the beginning, the frequency shift, Δf_0, is about 95 Hz. According to the Mindlin theory, this frequency shift corresponds to a radius of contact for a single glass sphere of about 500 nm. After the first cycle, Δf_0 is increased to the value of about 400 Hz. The Mindlin radius of contact increases about 2.1 μm. After shear-induced strengthening, the contact behavior during decrease and increase of the amplitude turns hysteretic. This effect is clearly visible in Fig. 19*a* and *b*. Arrows display direction of the drive level sweep.

(a) *(b)*

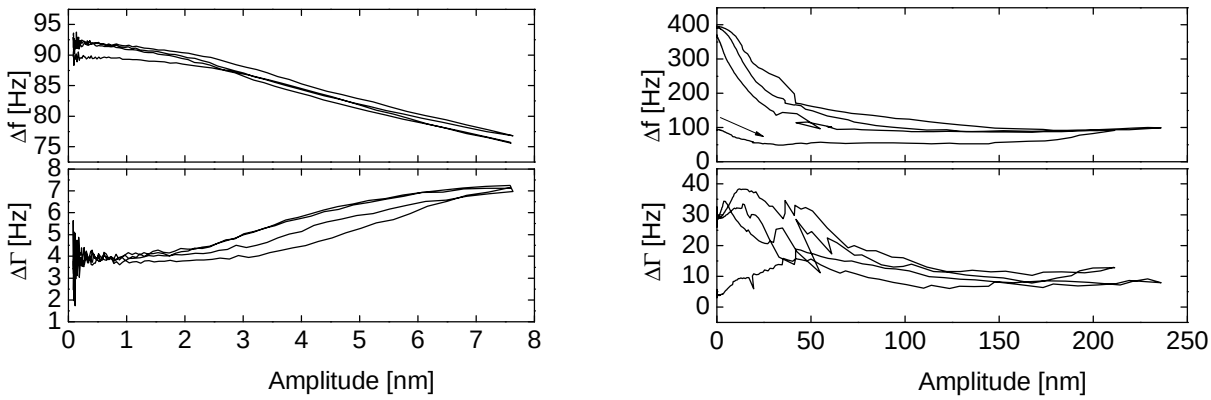

Fig. 18. Drive level results for glass spheres with the diameter of 700 μm, total mass of spheres and metal plate, is 1 g. (a) The relative humidity 9 %rH, drive level from –50 dBm to –10 dBm. (b) The relative humidity 6 %rH, drive level from –50 dBm to 20 dBm. An arrow shows start of the first drive level cycle. During this cycle, we observed shear-induced strengthening of the sphere–plate contact.

Further measurements were performed with humid air inside the box (Fig. 19*b*). We increased the relative humidity to 85–90 %rH. As mentioned in the works of Riedo et al. [22, 30] the stiffness of the contact due to capillary forces may depend on the contact time. For this reason, we waited for 12 hours in high humidity before the start of the measurements. With increasing humidity, the frequency shift, Δf_0 increased as well. The effect is the same as with single the Si_3N_4 sphere. Between the sphere and quartz surface, water bridges are created. As a consequence, the force between spheres and quartz crystal increases due to capillarity (Eq. 2.14). These capillary forces make a contribution to the increase in frequency shift. In humid atmosphere, a nonreversible behavior is clearly visible. The results obtained at a high humidity show very strong dependence on amplitude. With increasing relative humidity, the slope in Δf vs A curve increases. As a consequence, the characteristic length, λ_s, much decreases.

A next set of experiments was performed after drying the chamber. During the measurements, the humidity in the camber was lower than 35 %rH. Studies of adhesion force showed no dependence on humidity at humidities lower than 40 %rH [74, 75]. For the humidities lower than 40 %rH, the Kelvin radius (Eq. 2.10) is less than the atomic radius. Consequently, we can assume that for a humidity lower than 40 %rH, all the water is evaporated from the sphere–plate interface. We performed a series of experiments, where the maximum drive level was –10, 0, 10 and 20 dBm. The reason for gradually increasing the

maximum drive level was to probe the contact stiffness without removing sandcastle effect. It turned out that the strength of the contact is very high. With the highest drive level of 20 dBm, we reach an amplitude of about 5.5 nm. In this case a shear amplitude of 5.5 nm is not enough to remove the sandcastle effect or even weaken it, as for the single Si_3N_4 sphere (Fig. 11b). There is no dependence of Δf on the drive level. During the whole measurement, the frequency shift and the half bandwidth remain constant at 2730 Hz and 540 Hz, respectively (Fig. 20*b*). This result describes the sandcastle effect. The Mindlin radius of contact is much larger than what we had before.

(a) *(b)*

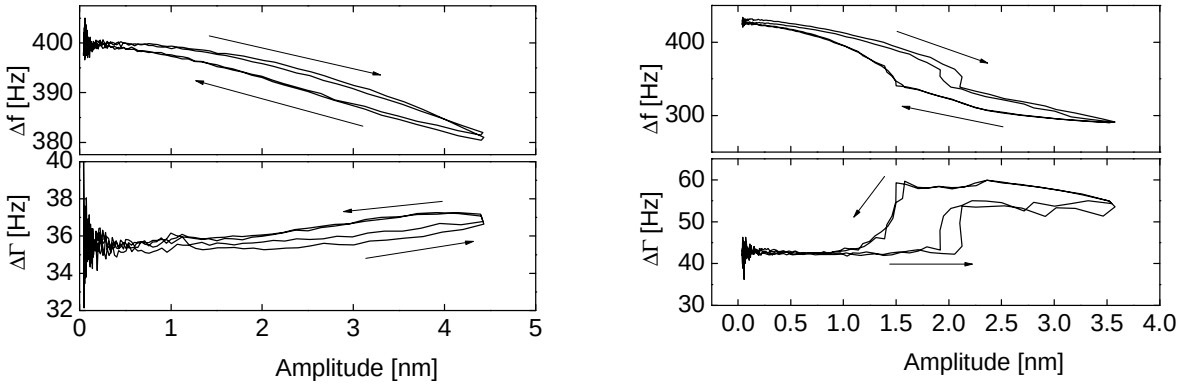

Fig. 19. Results for the glass spheres with the diameter of 700 μm and a total mass of spheres and metal plate of 1 g. Arrows on the graphs display direction of the drive level sweep. (a) After shear induced strengthening, humidity 6 %rH, drive level from –50 dBm to –10 dBm. (b) Humidity 85 %rH, drive level from –50 dBm to –10 dBm.

In Table 2 you can find the results of calculation based on the Hertz theory of elastic solids and the Mindlin theory of elastic contact under tangential shear force. All 20 spheres are assumed to be contact with the quartz surface. For the glass spheres, we used values of 62 GPa for the Young modules and 0.17 for the Poisson ration. For quartz we used 72 GPa and 0.23 for the Young modules and the Poisson ratio, respectively. We neglected with the gold electrode, science it is much thinner than the contact radius.

From Eq. 2.2, we calculate the Hertz radius, R_{Hertz}, of the contact between sphere and the quartz crystal. Using a linear fit function for the results with the glass spheres and applying (Eq. 3.15) from the Mindlin theory, we get spring constant $\kappa_{0,M}$, the static friction coefficient μ_s, the characteristic length λ_s, and the Mindlin radius of contact R_{Mindlin}.

Comparing the Hertz radius and the Mindlin radius of contact, we see that, initially, the Mindlin radius is smaller than the Hertz radius. In the initial dry state, the contact is made only across a few small asperities. After shear induced strengthening, the two surfaces find a more advantageous relative position. In the new position, the area of contact becomes higher than in the initial state before shear-induced strengthening. Without any normal force, we have an increase of area and a strengthening of the contact.

As discussed in the section 3.6, the static friction coefficient in the Mindlin model is proportional to the Mindlin radius, R_{Mindlin}, of contact and the characteristic length, λ_s. Analyzing the data from the table, we conclude that with increasing of humidity, the stiffness of the contact due to capillary forces of the water menisci increases as well. On the other hand, the presence of the water in contact area plays the role of a lubricant. As a consequence, small droplets of the water decrease the characteristic length and decrease the static friction coefficient.

Table 2. Calculation for glass spheres using the Mindlin theory. The number of spheres is 20, the total mass of the sample is 1 g, and the diameter of the spheres is 700μm

rH[%]	Δf_0[Hz]	$\Delta\Gamma$[Hz]	R_{Hertz}[μm]	R_{Mindlin}[μm]	λ_s[nm]	κ[kg/s^2]	μ_s
9	94	4	1.54	0.51	6.7	$0.62\ 10^6$	0.42
6	427	30	1.54	2.10	7.4	$2.8\ 10^6$	2.1
6	406	33	1.54	2.2	12.9	$2.7\ 10^6$	3.56
63	410	41	1.54	2.2	1.1	$2.7\ 10^6$	0.30
90	403	43	1.54	2.17	2.0	$2.7\ 10^6$	0.55
90	465	48	1.54	2.5	1.7	$3.1\ 10^6$	0.54
35	2730	560	1.54	14.5	–	–	–

One more thing we need to discuss is the plateau at the lowest amplitudes. The plateau is the part of the experimental results where there is no dependence of the frequency shift on the shear amplitude. There is no partial slip in this regime. This plateau is described with the Dybwad model. In this model, the frequency shift and the bandwidth shift are described by the Eq. 3.8.

We need to look careful to our graphs in the range of amplitudes below 5 nm. In Fig. 18*a* at amplitude below 2 nm, we have a small decrease in frequency. This part ascribe to the plateau. The reason for the small decrease is that our sample consists of 20 glass spheres. The sphere size is about 700 μm with a variability in the range of about 50 μm. The

spheres are mounted to the metal plate with double sides tape. The softness of the tape ensures that all spheres come into contact. However, variation in spheres size lead to different loads on the spheres. Some of the spheres have weak contact with the plate. Under lowest amplitude this weak contacts still have partial slip. These spheres with weak contact produce the small decrease in Δf. Still most of the spheres are in the Dybwad regime where no partial slip occurs.

Fig. 20*a* shows results for amplitudes lower than 10 nm obtained during strengthening initiated with a high shear amplitude. The dashed line shows the plateau. The width of the plateau is about 1 nm. Compared to the width of the plateau before strengthening, we see that the plateau has become smaller. In further measurement after strengthening of the contact the plateau have the same width of 1 nm. The increase of the humidity leads to a decrease of the plateau width (see Fig. 19*b*). For the sandcastle effect, as mentioned before, there is no dependence of the frequency shift on amplitude. Bandwidth and frequency shift are much higher than what we have without the sandcastle effect. As a consequence, maximum amplitude in our experiments is about 5 nm (see Fig. 20*b*). The contact between spheres and plate is hard. The sample and the quartz crystal accomplish an oscillation like a bulk medium. Such a contact is described with the Dybwad model in whole range of drive levels.

(a) *(b)*

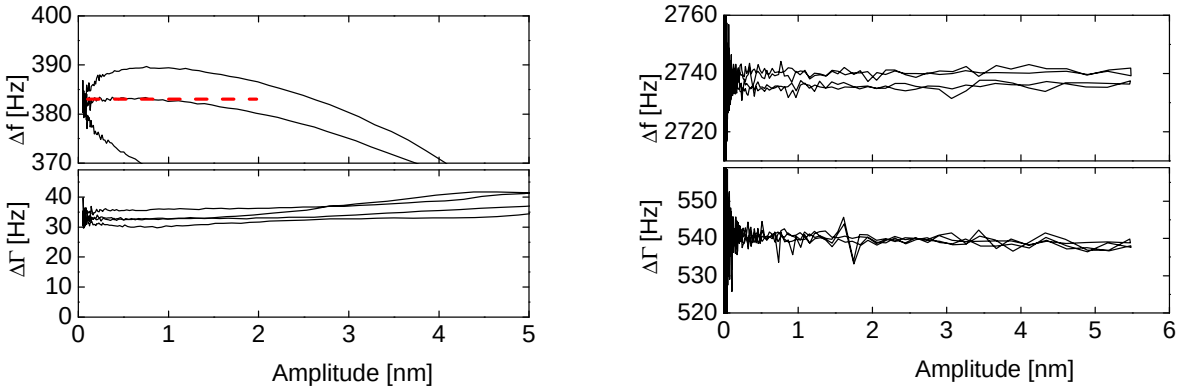

Fig. 20. Results on glass spheres with a diameter of 700 μm. The total mass of spheres and metal plate is 1 g. (a) Zoom for the measurement with humidity 6 %rH, after shear induced strengthening. The dashed line shows the plateau. (b) After dry–humid–dry cycle (sandcastle effect).

4.8. Glass spheres with a diameter of 225 μm

The next sample we have used consisted of glass spheres with a diameter of 225 μm. The number of glass spheres used to prepare the sample was 175.

We initially placed the QCM and the sample inside the plastic box and dried it to a relative humidity of 6 %rH. The sample and the QCM are not in the contact at this time. After drying we acquired the reference state for a bare crystal at a drive level 0 dBm.

Then, we placed the sample onto the quartz crystal and started the measurements. In the previous measurements with the single Si_3N_4 sphere and with the 700 μm glass spheres had we waited for 12 hours before starting the measurement. The reason for this was to exclude an influence of strengthening of the contact with the time ("relaxation processes"). The waiting time does not make any contribution to the strength of the sphere–plate contact after 12 hours. The relaxation process taking place after we place the sample onto QCM is much faster. It is enough to wait 30 min. The strength of the contact is constant after 30 min. Relaxation phase is outside the scope of the following chapter. With a waiting time of 30 min, we can be sure to have aging excluded from the experimental results.

As before, the first measurement was performed with a drive level lower than –10 dBm. With higher drive levels we would reach higher amplitudes and higher shear amplitudes, which would lead to shear-induced strengthening. The results of this measurement are shown in Fig. 21*a*. From 1 nm to 5 nm, the behavior is linear. This behavior is predicted by the Mindlin theory. Also, we expect a plateau at the lowest amplitudes. The discussion of the plateau at the lowest amplitudes follows later in this chapter. Subsequently, we have preformed a measurement with a maximum drive level of 20 dBm (Fig. 21b). A drive level of 20 dBm corresponds to an amplitude of about 200 nm. A shear amplitude of 200 nm initiates strengthening of the sphere–plate contact. The start of the measurement is labeled with an arrow. At the end of the first drive level cycle, the frequency shift, Δf_0, has increased from 155 Hz to 300 Hz. An increase of frequency shift, Δf_0, by two times corresponds to an increase of real contact area by a factor of 4 according to the Mindlin model. As for the glass spheres with bigger size, we observe hysteretic behavior during increase and decrease of the amplitude.

(a) *(b)*

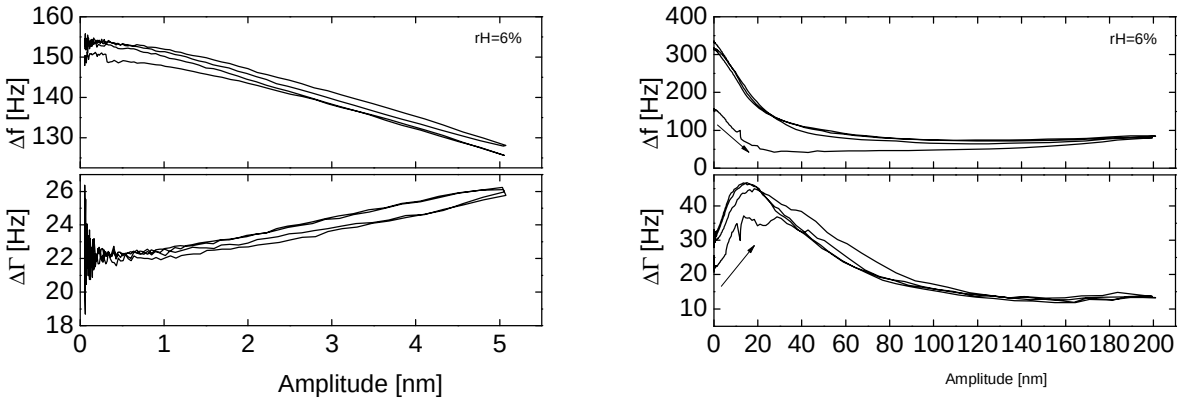

Fig. 21. Results for the glass spheres with the diameter of 225 μm. The total mass of spheres and metal plate is 1 g. (a) Humidity 6 %rH, drive level from –50 dBm to –10 dBm. (b) Humidity 6 %rH, drive level from –50 dBm to 20 dBm. An arrow shows the start of the first drive level cycle. During this cycle, one observes shear-induced strengthening of the sphere–plate contact.

Further measurements were performed with increased relative humidity inside the box. The results for this measurement are shown in Fig. 22*a*. Here, an interesting thing is observed. Following the increase of humidity, the frequency shift, Δf_0, decreases. A further measurement done at high relative humidity after a waiting time of 12 hours shows that the frequency shift, Δf_0, increased (Fig. 22*b*) in comparison with the results in a dry environment inside the box (Fig. 21*b*). A possible explanation is that with increasing humidity ring menisci arise around the points of contact. The water droplets in the contact area make a negative contribution to the frequency shift, Δf_0. At the same time, capillary forces gradually increase the normal force, and as a consequence, the strength of the sphere–plate contact increases.

The next steep of the experiment is drying of the environment inside the box. Measurements were performed inside the box with a relative humidity lower than 30 %rH and with a maximum drive level –10, 0, and 10 dBm. The reason for gradually increasing the drive level was not to destroy the sandcastle effect. At a drive level of 10 dBm, we observe partial removal of the sandcastle effect, 10 cycles completely destroy the sandcastle effect.

(a) *(b)*

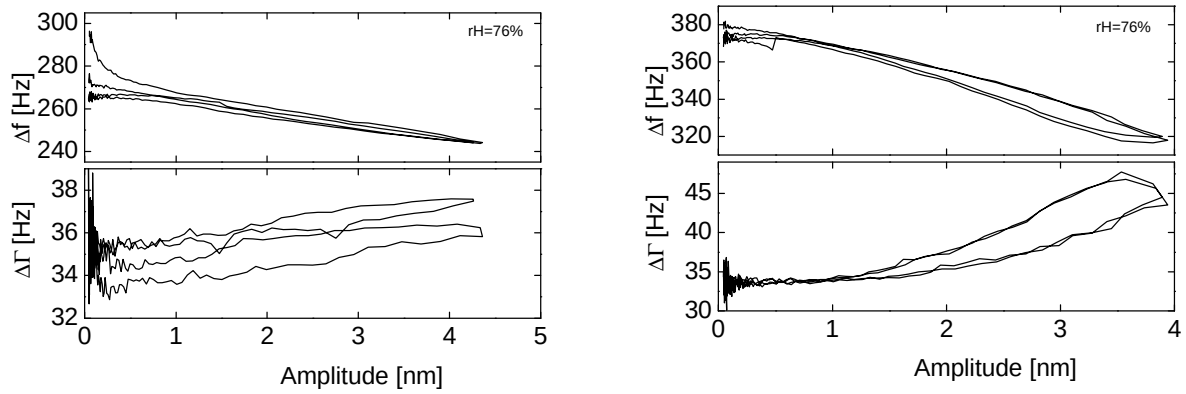

Fig. 22. Results for the glass spheres with the diameter of 225 μm. The total mass of spheres and metal plate is 1 g, drive level from –50 dBm to –10 dBm. (a) Measurements during increasing humidity inside the box and relative humidity 76 %rH at the end of the measure. (b) Humidity 76 %rH, after 12 hours waiting time.

Fig. 23*a* shows results for the sandcastle effect. Compared with the results for the bigger glass spheres, we see that the stiffness of the contact is smaller. The rather small bandwidth makes it possible to reach higher amplitudes with the same drive level. A higher amplitude will destroy the sphere–plate contact. The values of the frequency shift, Δf_0, in this measurement are similar to the ones found to the single Si_3N_4, sphere. In the measurements with a maximum drive level of –10 or 0 dBm, the sandcastle effect stays constant. There are no changes during the drive level cycles. Using a maximal drive level of 10 dBm, the amplitude of the quartz crystal reaches a value of about 30 nm. This shear amplitude partially destroys the contact between spheres and plate. These results you can see in Fig. 23*b*. The start of the measurement is labeled with an arrow. We observe a decrease in frequency shift, Δf_0, after the first and the second cycle. We have not tried to use higher values for the drive level. From previous experience, we know that higher values destroy the sandcastle effect during the first cycle. After removing of sandcastle effect the behavior of frequency shift and HBHW corresponds to the initial results which we have before the dry–humid–dry cycles.

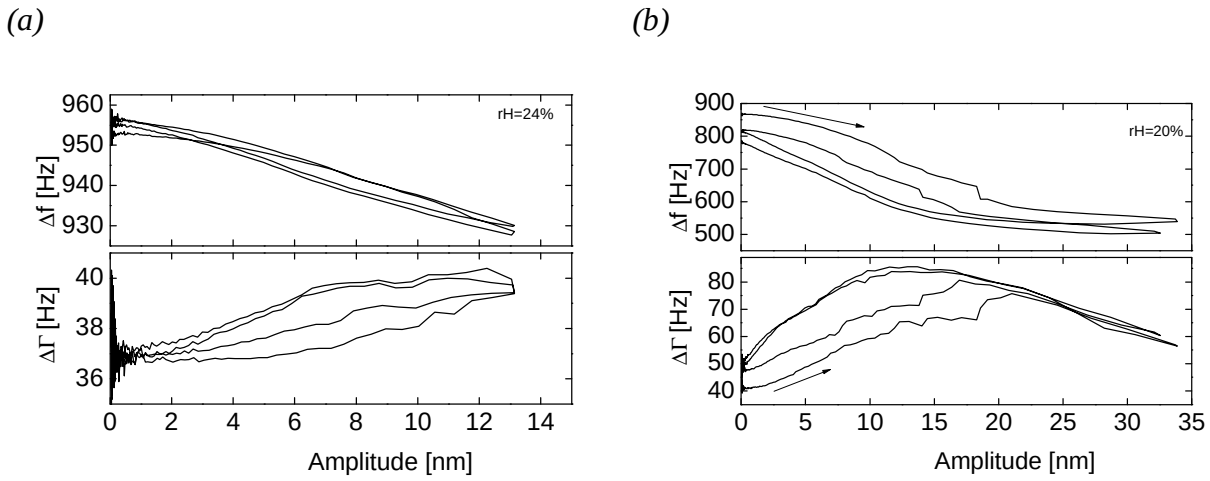

Fig. 23. Results for the glass sphere with the diameter of 225 μm. The total mass of the spheres and the metal plate is 1 g. (a) Sandcastle effect, humidity 24 %rH, drive level from –50 dBm to 0 dBm. (b) Sandcastle effect and its partial removal, humidity 20 %rH, drive level from –50 dBm to 10 dBm. An arrow shows the start of the first drive level cycle. During this cycle, one observes a weakening of the sandcastle effect.

Using Eq. 2.4 from the Hertz theory of elastic contact we calculate the Hertz radius of contact. The frequency shift, Δf, in the Mindlin theory depends linearly on amplitude (Eq. 3.15). Applying a linear fit to the experimental results, we calculate the Mindlin radius, R_{Mindlin}, the spring constant, κ, and the static friction coefficient, μ_s. For the calculation we have used the assumption that all 175 glass spheres of the sample touch the surface of the crystal. The Young modulus and the Poisson ratio for the glass sphere are 62 GPa and 0.17 respectively. For the quartz crystal the values are 72 GPa and 0.23. We have neglected the gold electrode science it is much thinner than the contact radius. A summary of the experimental data and the calculations using the Hertz and Mindlin theory are shown in Table 3.

The first two rows show the results obtained before shear-induced strengthening. Comparing the Hertz and the Mindlin radius, we see that Mindlin radius of contact is more than five times smaller. There are two possible explanations. Firstly, we can make the assumption that not all glass spheres touch the surface of the quartz crystal. In a real situation, some of the spheres will not be in contact with the surface and therefore do not take part in the motion. The second explanation is based on the hypothesis that the real area of the contact is smaller than predicted by the Hertz theory.

Within the Hertz theory, sphere and plate have a circular contact area with a radius given by Eq. 2.4. Due to the roughness of surfaces, not the whole area is in contact. We expect our results probe the real contact area.

Table 3. Calculation for glass spheres using the Mindlin theory. The number of spheres is 175, the total mass of the sample is 1 g, and the diameter of the spheres is 225μm.

rH[%]	Δf_0[Hz]	$\Delta\Gamma$[Hz]	R_{Hertz}[μm]	$R_{Mindlin}$[μm]	λ_s[nm]	κ[kg/s^2]	μ_s
06	160	21	0.51	0.10	4.1	1.06 10^6	0.44
06	158	22	0.51	0.10	4.5	1.05 10^6	0.48
06	340	30	0.51	0.21	6.2	2.26 10^6	1.43
06	355	32	0.51	0.22	5.8	2.36 10^6	1.40
06	366	34	0.51	0.23	10	2.44 10^6	2.49
76	374	35	0.51	0.23	3.4	2.50 10^6	0.86
76	387	33	0.51	0.24	3.9	2.58 10^6	1.03
76	386	33	0.51	0.24	3	2.58 10^6	0.79
28	915	48	0.51	0.56	131	6.10 10^6	81
26	938	42	0.51	0.58	130	6.26 10^6	83
24	960	37	0.51	0.59	69	6.40 10^6	45
22	817	50	0.51	0.50	7.3	5.45 10^6	4.05

4.9. Glass spheres with the diameter of 112 μm

A further series of experiments was performed with glass spheres with a diameter of 112 μm. This size is so small that the exact number of spheres cannot be determined exactly. The number is about 300

From Eq. 2.2, the Hertz radius of the sphere–plate contact for a single sphere is calculated as about 330 nm. This value is comparable with the maximum shear amplitude, which can be reached with our experimental setup. For the samples with a diameter of 700 μm and 225 μm we observe shear induced strengthening of the sphere–plate contact. For

the spheres with a diameter of 112 μm, shear strengthening is already achieved with an amplitude of about 15 nm (Fig. 24*a*). An arrow labels the beginning of the measurement. After the first cycle, the frequency shift, Δf_0, increases from 600 Hz to 700 Hz. For the bigger spheres this effect is much stronger. In case of the spheres with the diameter of 700 μm, the frequency shift, Δf_0, increases up to 4 times.

At the maximum drive level of 20 dBm, we reach an amplitude about 300 nm. In this case, the shear amplitude is comparable with the radius of contact, which leads to a decrease of the frequency shift, Δf_0. The real area of contact has become smaller. When the shear amplitude is much smaller than the radius of contact, it only leads to small shift of the spheres relative to the surface. With such a small shift, the real area of the contact becomes larger. In the new position, the contact becomes stronger and the particles can not move away from this position. This new position is more advantageous for the spheres.

When the shear amplitude is comparable with radius of contact, energy of shear is high enough to prevent a movement of the spheres to a position. In this new position the frequency shift, Δf_0, would become smaller than after shear-induced strengthening of the contact (Fig. 24*b*). An arrow labels the beginning of the experiment. A decrease of the frequency shift implies that the Mindlin radius of contact has become smaller. At the same time, the static friction coefficient, μ_s, has become larger. This makes the new position stable in further drive level cycles. These new location have a smaller area of contact than we had before, but the resistance to the high frequency oscillatory shear has increased.

We can explain this, using the analogy of the potential well. The initial positions of the spheres are close to the wall of the potential well. Under high shear we initiate a movement down to the center of the well. There, the spheres are in a stable position. Further measurements with this amplitude can not change the positions of the spheres in the well. If we increase the amplitude further, the shear energy becomes so large that the spheres leave well and find new a place in another potential well.

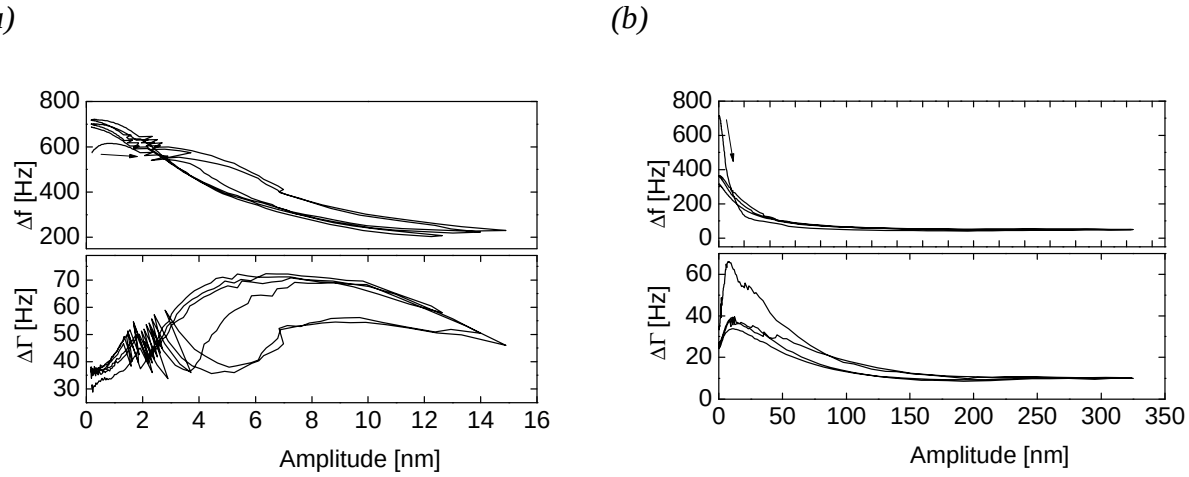

Fig. 24. Results for the glass sphere with a diameter of 112 μm and a total mass of spheres and metal plate of 1 g. The relative humidity during the measurements is 13 %rH. (a) Shear induced strengthening of the contact, drive level from –40 dBm to 0 dBm. An arrow shows the start of the first drive level cycle. During this cycle, one observes shear-induced strengthening. (b) Shear-induced weakening of the contact, drive level range: –40 dBm to 20 dBm. An arrow shows the start of the first drive level cycle. During this cycle, one observes weakening.

Fig. 25*a* shows results obtained after shear-initiated strengthening and weakening of the sphere–plate contact. On this image, we observe a plateau at amplitudes lower than 2 nm. The dashed line on the graph is a linear fit according to the Mindlin theory. From the coefficients of the fit, we can calculate the spring constant, κ, the static friction coefficient, μ_s, the characteristic length, λ_s, and the Mindlin radius of contact, R_{Mindlin}. A summary of the experimental results and the calculation with the Hertz and Mindlin theory is given in Table 4. In the second row we see that the frequency shift, Δf_0, decreased, but that the static friction coefficient increases at the same time.

Fig. 25*b* shows results taken after we have increased the humidity inside the plastic box and waited for about 12 hours before the start of the measurement. With increasing humidity, we have an increase in the frequency shift, Δf_0. The calculation for this experiment is shown in the third row of Table 4. Comparing these numbers to the dry state, we see that the Mindlin radius of contact for the humid state has increased. As discussed before, we find menisci around the contact points and liquid bridges between asperities under high humidity conditions. The capillary force increases the stiffness of the contact and real area of contact. The presence of the liquid on the quartz crystal surface decreases the frequency. That means that the calculation made with the Mindlin theory only provides approximate values of the Mindlin radius of sphere–plate contact. Getting back to the Table 4, the static friction

coefficient is much smaller than we have in the dry state. On the one hand, menisci or liquid bridges increase the normal force and the area of contact. This might lead to an increase of the friction coefficient. On the other hand, the presence of the liquid in the contact plays a role of lubricant which decreases the friction coefficient.

The next steep is drying of the chamber and performing measurements in dry conditions. During the measurement, the humidity inside the box was lower than 30 %rH. With a relative humidity lower than 40 %rH, the Kelvin radius (Eq. 2.10) becomes smaller than the atomic size. Therefore, we expect that all water is evaporated from the area of contact. As before, we observe the sandcastle effect. We have a large increase in frequency shift, Δf_0, and bandwidth, $\Delta\Gamma_0$. As in the previous measurements with the bigger spheres, we performed several experiments. In this experiment we have used a maximum drive level of –10, 0, and 10 dBm. The drive level of 10 dBm destroys the sandcastle effect. The fourth row in Table 4 displays the results for the sandcastle effect. The frequency shift, Δf_0, is similar to the shift for the glass spheres with the diameter of 700 μm. With the big spheres, it was not possible to remove the sandcastle effect at the maximum drive level. Even with a drive level of 20 dBm, the sandcastle stayed stable. For small, the spheres sandcastle falls at a drive level of 10 dBm. The explanation for this finding is that the bigger spheres have a small number of sphere–plate contacts, but the area of these contacts is larger than for the small spheres. With smaller spheres we have many sphere–plate contacts, but these contacts are small. Larger contacts are more stable under tangential shear motion than many small contacts.

(a) *(b)*

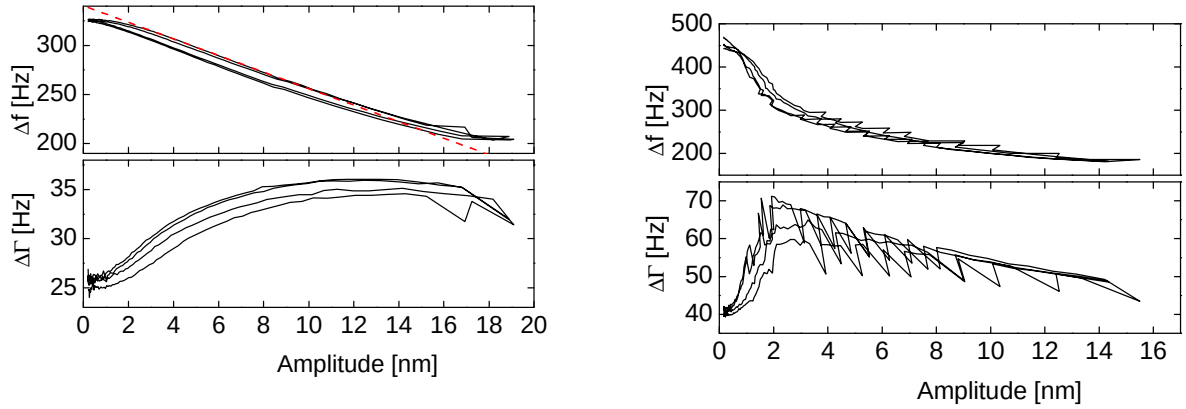

Fig. 25. Results for glass spheres with a diameter of 112 μm and a total mass of spheres and metal plate of 1 g. (a) The relative humidity is 10 %rH, drive level range: –50 dBm to 0 dBm. The dashed line is a linear fit. (b) The relative humidity is 84 %rH, drive level from –50 dBm to 0 dBm.

A summary of the results and calculation is shown Table 4. In the sample preparation we have used about 300 glass spheres. In our calculations we have used the approximation that all 300 spheres are in contact with the surface. The Young modulus and the Poisson ratio for the glass sphere are 62 GPa and 0.17, respectively. For quartz crystal the respective values are 72 GPa and 0.23. We have neglected the gold electrode science it is much thinner than the contact radius.

In the first row, we show the results after obtained shear-induced strengthening. For this sample, we do not have data from strengthening of the contact, because we have used a maximal drive level of –10 dBm. During the first cycle, we observe a strengthening of the contact. Then, we increased the drive level to the maximum. At the maximum drive level with a shear amplitude of 300 nm, we observe weakening of the contact. These results are presented in the second row. The third row concerns the glass spheres in humid atmosphere. The fourth line shows results taken in presence of the sandcastle effect, when we have a large increase of frequency and bandwidth. The fifth and sixth line show data, where the sandcastle is destroyed.

Table 4. Calculation for glass spheres using the Mindlin theory. The number of spheres is 300, the total mass of the sample is 1 g, and the diameter of the spheres is 112 μm.

No	rH[%]	Δf_0[Hz]	$\Delta\Gamma$[Hz]	R_{Hertz}[μm]	R_{Mindlin}[μm]	λ_s[nm]	κ[kg/s^2]	μ_s
1	13	778	36	0.39	0.28	1.5	5.19 10^6	0.79
2	13	329	25	0.39	0.12	6.6	2.2 10^6	1.48
3	84	497	40	0.39	0.18	0.89	3.3 10^6	0.30
4	30	2864	310	0.39	1.03	12	19.1 10^6	23.39
5	9	396	30	0.39	0.14	3.1	2.64 10^6	0.83

4.10. Effect of added mass in experiments using glass spheres with a diameter of 700 μm

As discussed before, one can measure the Mindlin radius of the contact between sphere and plate by drive level measurements. We expect that the Mindlin theory should provide the real area of contact. Using experimental data it is possible to calculate the static friction coefficient and other parameters of the system.

We have used glass spheres to study how all the parameters from the Mindlin model depend on the normal force. In this part we have used spheres with a diameter of 700 μm. The number of spheres was 20. During the experiment the relative humidity inside the box was less than 10 %rH. Before placing the sample onto the quartz crystal, we determined the reference state for the bare crystal at a drive level of 0 dBm. All measurements were performed with the drive level up to –10 dBm. This low drive level avoids shear strengthening.

Fig. 26*a* presents results for spheres with a total mass of the sample 1g. We placed the sample onto the crystal and started the measurement. The beginning of the measurement is labeled with an arrow. During the first cycle, the frequency shift increases. The reason for this increase is a relaxation in the contact that takes place when we place our sample on the quartz surface. More information about this relaxation can be obtained from further time scale measurement with constant drive level. If we wait 30 min between placing the sample on to the crystal or adding the mass we have results like ones shown in Fig. 26*b*. In this figure, there is no relaxation of the contact.

In the results, there is no clear plateau at low amplitudes. On the contrary, there even is a small decrease in the Δf_0 at the smallest amplitude. A more clear plateau is visible in the

bandwidth shift. As we know, the existence of plateau means that we are in the Dybwad regime, where there is no partial slip. Our sample consists of 20 glass spheres mounted to a metal plate with the double side tape. The soft backing ensures that all spheres come into contact with the crystal. But still, some of the spheres are in weak contact. Even for the smallest amplitudes, these weak contacts lead to partial slip. We can assume that in the amplitude range below 2 nm, some spheres are without partial slip.

Secondly, we find that we in a good agreement with the Mindlin theory. At a shear amplitudes above 2 nm, we see a nice linear behavior. The dashed in Fig. 26*b* line shows the linear fit.

Finally, the behavior with increasing and decreasing of amplitude is the same. There is no hysteretic behavior in the drive level measurements.

(a) *(b)*

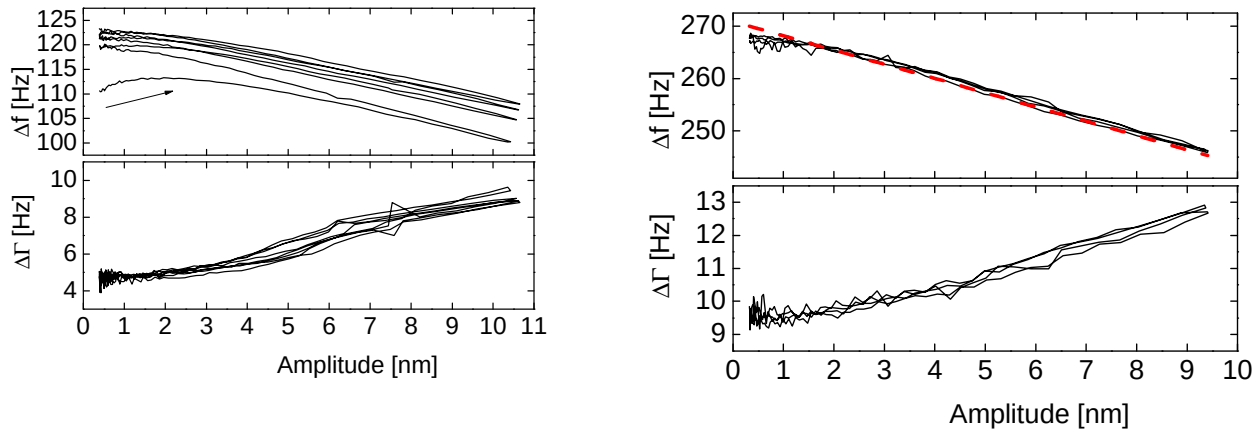

Fig. 26. Results obtained on the glass spheres with a diameter of 700 μm. The relative humidity during the measurements is 9 %rH. The drive level range is –40 to –10 dBm. (a) Total mass of the sample with spheres of 1 g. (b) Total mass of the sample and added mass of 5.2 g. The dashed line shows a linear fit for the frequency shift.

A summary of the results and the calculations is shown in the Table 5. We started with a mass of 1g. For every further measurement, we added a mass of about 0.4g on top of the sample.

From this table, we can compare the theoretical results for the Hertz radius of contact and the experimental results from Mindlin theory. The Mindlin radius of contact is smaller than the Hertz radius. As usual the real area of contact is smaller than the area predicted by the Hertz theory. In the Hertz theory, the radius of contact depends on the load as $P^{2/3}$. From

our experimental data we, see that the Mindlin radius of contact increases faster with the load than in Hertz theory. As consequence, real area of contact increases faster than predicted by Hertz model.

In the experimental results, there is no obvious dependence of the characteristic length, λ_s, on the shear amplitude. This implies that with increase of the vertical load the frequency shift, Δf_0, increases as well, but there is no systematic trend in the amplitude dependence of Δf. In the further calculation for the static friction coefficient, this leads to decrease of the friction coefficient with increased load.

Table 5. Table of results for the sample with the added mass. The number of spheres is 20, the diameter is 225μm, the relative humidity during the measurements was lower than 9 %rH.

No	*m*[g]	Δf_0[Hz]	$\Delta\Gamma_0$[Hz]	λ_s[nm]	κ[kg/s2]	μs	R_{Hertz}[μm]	$R_{Mindlin}$[μm]
1	1	124	5	12	$0.8\ 10^6$	0.96	1.57	0.67
2	1.4	132	6	17	$0.9\ 10^6$	1.04	1.75	0.71
3	1.8	150	6	13	$1.0\ 10^6$	0.72	1.89	0.81
4	2.3	154	6	20	$1.0\ 10^6$	0.89	2.05	0.83
5	2.7	140	5	24	$0.9\ 10^6$	0.83	2.16	0.76
6	3.1	173	6	20	$1.15\ 10^6$	0.75	2.26	0.9
7	3.6	250	10	14	$1.6\ 10^6$	0.65	2.38	1.35
8	4.0	242	9	15	$1.6\ 10^6$	0.6	2.46	1.3
9	4.4	232	8	20	$1.54\ 10^6$	0.71	2.54	1.25
10	4.8	259	9	15	$1.73\ 10^6$	0.54	2.61	1.39
11	5.2	270	9	17	$1.8\ 10^6$	0.6	2.68	1.45

As mentioned before, after placing the sample on the crystal or adding mass, there is a relaxation. To observe this effect, we have performed measurements as a function of time with a constant drive level of –20 dBm. We have used a small drive level to prevent a possible influence of the shear amplitude on the sphere–plate contact. At the same time –20 dBm is high enough to have a stable result. The results of the experiment are shown in Fig. 27. In this figure, the label “1” indicates the moment when the sample was placed on to

the quartz crystal. Numbers 2–8 label the moments when we have added mass. The numbers corresponds to the masses given in Table 5.

When we add mass, the frequency usually first decreases. This is caused by the addition of the mass. When placing the mass onto the crystal, we create additional stress in the sphere–plate contacts. In some cases, (points 5 and 7 in the Fig. 27) the additional stress induces an increase of frequency. Subsequently the frequency, *f*, rises slowly. In the frame of the Mindlin model, we can interpret the increase in Δf as an increase of the Mindlin radius of contact. As a consequence we, observe an increase of the area of contact. The kinetics has exponential character. Such a behaviour of the area of contact can be described with Eq. 2.18. Applying an exponential fit function ($\sim \exp(-t/\tau)$) to the results, we can find the characteristic time, τ. The characteristic time is about 2 minutes.

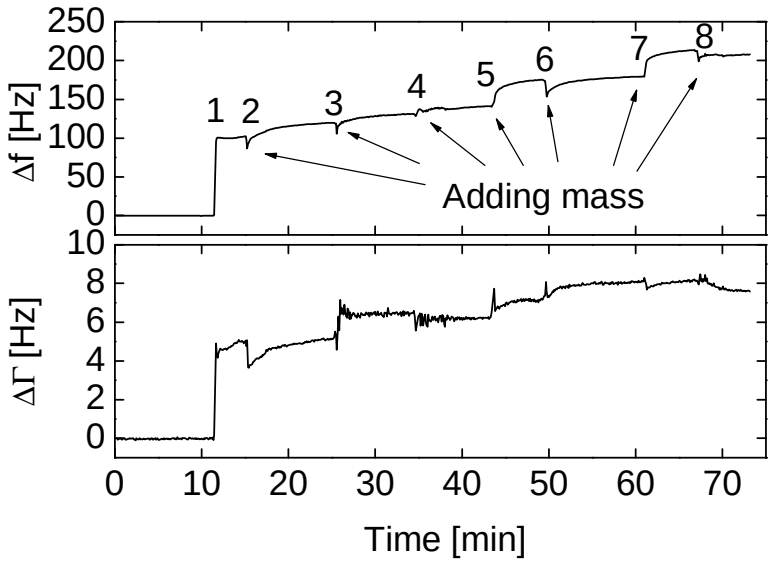

Fig. 27. The results for frequency shift and bandwidth shift versus time for glass spheres with the diameter of 700 μm. The drive level is –20 dBm. The relative humidity during the measurement is less than 9 %rH. Point "1" is the time when the sample was placed onto the crystal. Points 2 to 8 are the times when mass was added.

4.11. Effect of added mass in experiments using glass spheres with a diameter of 225 μm

From Hertz theory we know that the radius of contact between sphere and plate depends on the normal force. From the drive level measurements the Mindlin radius of

contact is available via the frequency shift, Δf_0. Increasing the mass of the sample, we observe a dependence of the Mindlin radius on the normal force. Afterwards, we can compare the radius of contact from Mindlin and Hertz theory. The Mindlin theory makes it possible to calculate the static friction coefficient, μ_s, and the spring constant, $\kappa_{0,M}$, of the sphere–plate system under high frequency oscillatory shear motion. And then find how these parameters depend from the normal force.

In this part, we used a sample with glass spheres of 225 μm in diameter. The number of spheres was 175. Before placing the sample to the quartz crystal, we determined the reference state for bare crystal at a drive level of 0 dBm. In order to increase the normal force, we added on the top of the sample small plates with a mass of about 0.4 g each. During the experiments, the relative humidity inside the box was below 9 %rH. The measurements were performed with a drive level from –40 dBm up to –10 dBm. The drive level of –10 dBm is enough to observe the plateau and transition to the Mindlin regime of partial slip. Higher drive levels may cause a strengthening of the sphere–plate contact induced by the shear movement. Strengthening of the contact is outside the scope of this chapter.

From the results with the glass spheres with a diameter of 700 μm we know, that after we have placed the sample or increased the normal force, there is a relaxation effect. We will discuss his effect in the context of further results for the frequency shift in time scale with the constant drive level. The relaxation effect prevents us to watch plateau. To exclude this, we have to wait for 30 minutes after addition of the sample or increasing the normal force. This time is enough for the sphere–plate contact to reach a stationary state.

Fig. 28*a* and *b* are the results for the glass spheres wit a total mass of sample 1 g and 5.2 g respectively. Other results with the mass from 1 to 5.2 g are similar to these.

In Fig. 28*a*, we do not see a clear plateau at lowest amplitudes. At amplitudes lower than 1 nm decreasing in frequency shift is very slow. The sample is prepared from 175 glass spheres mounted to the metal substrate with the double-sided tape. The soft backing ensures that all spheres come into contact with the quartz crystal. A small part of the spheres are in weak contact with the crystal. This weak contact induces partial slip even at the lowest amplitude range. The plateau in the results means that our spheres are in the point contact regime, where there is no partial slip. Partial slip gives us small decrease of the frequency in the lowest amplitudes. Therefore, a small increase in frequency shift is the result of partial slip from those spheres which have a weak contact with the crystal. We can conclude that at amplitudes below 1 nm, some spheres should be without partial slip. With the dash–doted

line, we have labeled the plateau. The dashed line shows a linear fit function according to the Mindlin model.

Fig. 28*b* shows with the results with a total mass is 5.2 g of the sample and added mass. At the lowest amplitudes we have small decrease of the frequency shift. We can sea a plateau in this figure. The width of the plateau becomes smaller with increasing normal force.

(a) *(b)*

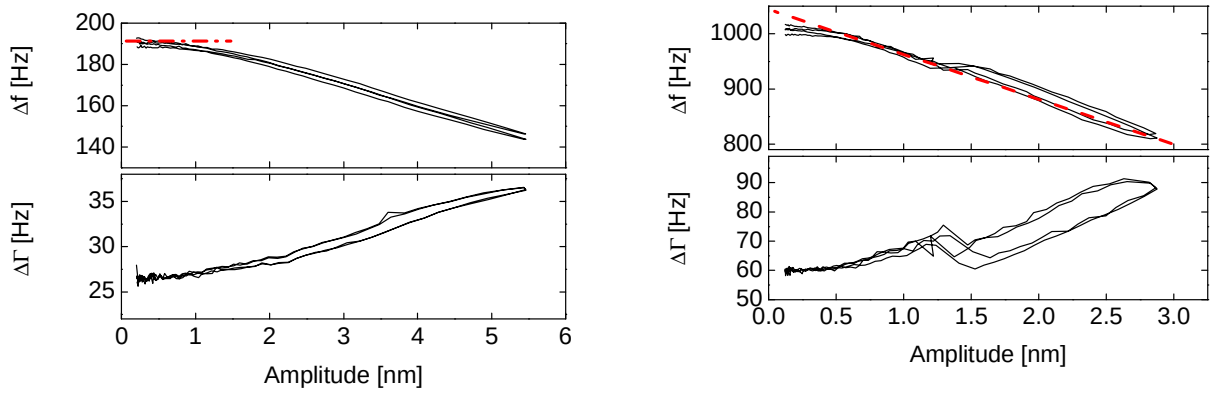

Fig. 28. Results for glass spheres with the diameter of 225 μm. The relative humidity during the measurements is 9 %rH. The drive level ranges from –40 to –10 dBm. (a) Total mass of the sample with spheres is 1 g. The dashed line is linear fit. The dash–doted line labels the plateau. (b) Total sample mass is 5.2 g. The dashed line shows the linear fit for the frequency shift.

A summary of the results and calculations for the mass from 1 g to 5.2 g with the steep about 0.4 g is shown in the Table 6. From this table, we can compare results for the Hertz radius and the Mindlin radius of elastic sphere–plate contact. For different normal forces, the Hertz radius is larger than what we have from the calculation of the Mindlin radius. This is one more demonstration that the real area of contact is smaller than what is predicted with the Hertz theory. From the result we can conclude that increasing of the Mindlin radius is similar to what we have to the Hertz radius (Fig. 29).

Getting back to the Table 6, we observe that the static friction coefficient, μ_s, slightly decrease with the increasing mass. With increasing normal force, the slope in the plot of the frequency shift, Δf, versus amplitude becomes larger. This is slightly different from the results found for the bigger spheres. For the bigger spheres, the slope in the frequency shift, Δf, is much smaller. The bandwidth, $\Delta\Gamma_0$, increases with the mass. Increasing of the mass

from 1 g to 5.2 g increases the bandwidth increased two times. The same behavior of the bandwidth was observed for the bigger glass spheres.

Table 6. Table of results for a sample with added mass. The number of spheres is 175, the diameter is 225μm, the relative humidity during the measurements was below 9 %rH.

No	m[g]	Δf_0[Hz]	$\Delta\Gamma_0$[Hz]	λ_s[nm]	κ[kg/s2]	μs	R_{Hertz}[μm]	$R_{Mindlin}$[μm]
1	1	202	26	3.1	$1.34\ 10^6$	0.4	0.52	0.12
2	1.4	272	30	2.8	$1.81\ 10^6$	0.4	0.58	0.16
3	1.8	374	33	2.3	$2.5\ 10^6$	0.32	0.62	0.23
4	2.3	537	45	1.9	$3.6\ 10^6$	0.29	0.68	0.33
5	2.7	601	47	2.1	$4.0\ 10^6$	0.31	0.72	0.37
6	3.1	669	48	1.9	$4.46\ 10^6$	0.27	0.75	0.41
7	3.6	730	50	1.8	$4.8\ 10^6$	0.24	0.79	0.45
8	4.0	792	51	2.1	$5.3\ 10^6$	0.27	0.82	0.49
9	4.4	897	57	2.3	$6.0\ 10^6$	0.31	0.84	0.55
10	4.8	962	57	2.2	$6.4\ 10^6$	0.3	0.86	0.59
11	5.2	1045	59	2.0	$7.0\ 10^6$	0.27	0.89	0.64

Fig. 30 shows the results for frequency shift and bandwidth shift versus time. In this figure, we can observe a relaxation effect, which takes place after we add the sample or increase the normal load. During the measurement, we have added sample and then increase the load with small glass plates with a mass about 0.4 g. The label “1” indicates the moment when we have placed the sample to the crystal. Numbers 2 to 11 label the moment of increase of the load. A drive level of –20 dBm was used in this measurement. With this drive level, we have a stable result for frequency and bandwidth. –20 dBm correspond to the shear amplitude of about 3 nm. The shear amplitude of 3 nm is small enough to prevent an influence of the shear movement on to the sphere–plate contact.

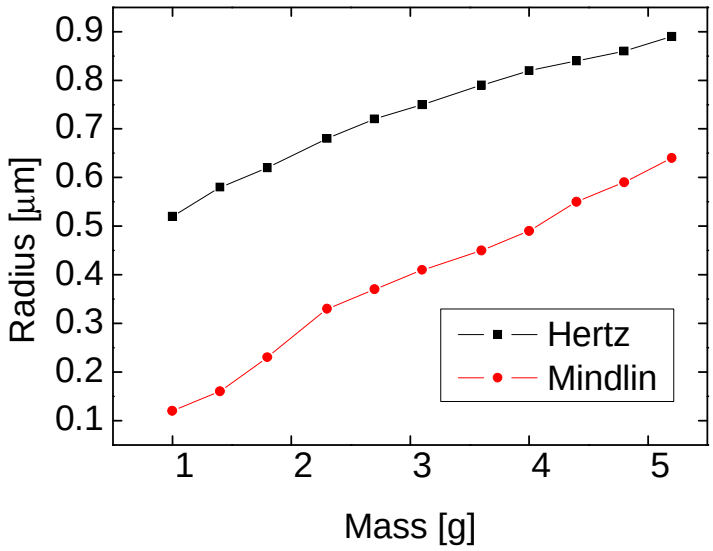

Fig. 29 The Hertz radius (squares) and the Mindlin radius (circles)of elastic conrtact versus added mass. A glass spheres with a diameter 225 μm. The number of spheres is 175.

When we add the mass the frequency shift could increase or decrease. The reason for the increase is the increase of the load. The decrease is a result of the rearrangement of the load between different spheres at the moment when we adding the mass on top of the sample. Afterwards, we observe an increase of the frequency shift, Δf, with time. These increases of the frequency shift, Δf, describe increase of the Mindlin radius of contact vs time. As a consequence increase the area of contact. These results are in agreement with the observations by references [86, 87, 88]. These references report a quasi–logarithmic growth of the contact area with the "age" of interface, *i.e.* with the time of contact. Such a behavior of increase of the contact area predicted with Eq. 2.18. The increase of the frequency versus time after increase the load, we term in the work as the relaxation effect in the sphere–plate contact. The characteristic time, τ, from the exponential fit ($\sim\exp(-t/\tau)$) found to be about 2 minutes. This time coincides with the characteristic time for the bigger glass spheres. From this we can suppose that characteristic time depends on the nature of the bodies in the contact.

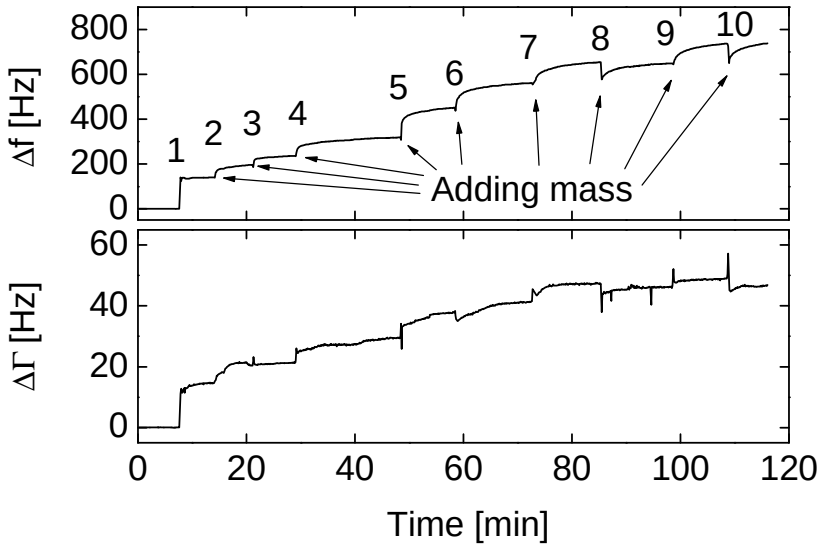

Fig. 30. Results for frequency shift and bandwidth shift versus time for glass spheres with a diameter of 225 μm. The drive level is –20 dBm. The relative humidity during the measurement is 7 %rH. Point 1 is the point of the time when have added the sample on the crystal. Points 2 to 11 are time points when we have added mass.

4.12. Sandcastle effect

From childhood, all of us know that the physical properties of wet and dry sand are different. From wet sand one can to build different figures or simply sandcastles. It is impossible to make the same things from dry sand, because the construction from dry sand is unstable. After drying a sandcastle, it stays stable or even becomes stronger.

The contact between solids is a complex problem which involves mechanical properties of the material and the geometrical characteristics of the surfaces. The mechanics of granular media or mechanics of small objects is still under investigation. Much attention of research is focused on dry granular media. Much less investigated are granular media with a small amount of added fluid or in high humidity conditions. An open question is what occurs while drying or decreasing the humidity in contacts between particles in granular media.

By studying the contact between a single sphere or multiple spheres with the QCM, we try to understand and describe what happens with granular media in the wet state or in a humid atmosphere and after drying. The shifts in frequency and bandwidth were used to infer the different parameters of the sphere–plate contact. A strong increase in frequency shift after

a dry–wet–dry cycle was attributed to an increase of the stiffness of the sphere–plate contact. This increase of stiffness was called “sandcastle effect”.

The interpretation of the sandcastle effect is based on capillary forces arising from liquid condensing at the points of contact or between two points of contact situated not far away from each other. The drying process increases the strength of the contact. The capillary forces depend on humidity, contact angle, surface roughness, time, and other parameters. Fig. 31 depicts the processes which we believe to occur.

In the initial dry state the contact between the surfaces is made across few, small contact points (Fig. 31*a*). These points of contact transport little stress and have a small influence on the resonance frequency. With higher amplitude shear oscillations, the two surfaces find more advantageous positions (Fig. 31*b*), and also undergo small elastic deformations. The amplitude of quartz crystal is no more than several hundreds nanometers. In the new positions, the number of asperities in the contact area increases. With increasing humidity, we find ring menisci around the contact points. When the Kelvin radius exceeds the scale of the surface roughness, new liquid bridges form between asperities that were initially not in contact (Fig. 31*c*). The capillary force and the water bridges make a contribution to the normal force and increase the shear stiffness. The increase of shear stiffness has an influence on the resonance frequency. At the same time, the presence of the liquid in the contact area also makes a contribution to the resonance frequency shift due to its mass. The increase of stiffness ($\Delta f_0>0$), and the increase of the liquid volume ($\Delta f_0<0$) partially compensate each other. For this reason, we do not see big changes while increasing the humidity.

While decreasing the humidity and drying the menisci, the radius of curvature is decreased. As a consequence, the Laplace pressure (Eq. 2.11) increases. This elastically deforms the surface into having greater area of contact and increases the number of contact points (Fig. 31*d*). This phenomenon of stiffness increase we call sandcastle effect. The sandcastle effect was previously described by Halsey [68] and Schiffer [69]. These two papers describe the sandcastle effect in the wet state. The phenomena discussed here take place after drying of the sphere–plate contact.

Another possible explanation of the sandcastle effect is the formation of salt bridges after drying of the water at the point of contact. To rule out this hypothesis, we made series of experiments with organic solvents. Salts are insoluble in organic solvent. In this way we can exclude influence of salts on the stiffness of the sphere–plate contact.

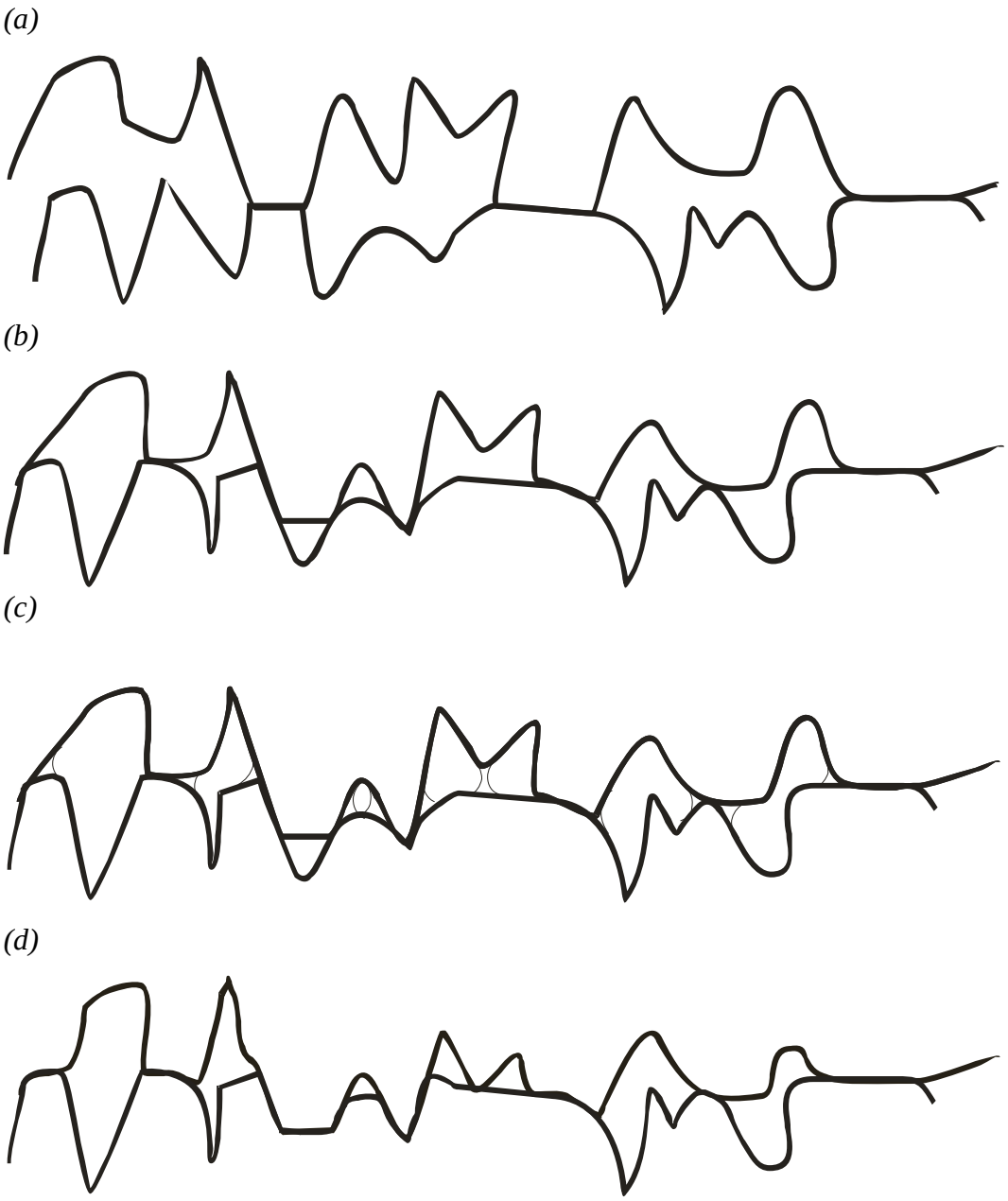

Fig. 31. Schematic drawing of the contact zone between sphere and quartz crystal surface. (a) Contact is made across small asperities. (b) After shearing, the two surfaces come closer to each other, which leads to increased area of contact and, as a consequence, an increase in the strength of contact. (c) With increased humidity, the wet volume increases and water bridges form. (d) Drying of the meniscus and water bridges deform the surface and increase the area of contact.

4.13. Conclusion

We have performed a series of experiments with a single Si_3N_4 sphere and with glass spheres. We have used glass spheres of different size and different numbers in the sample preparation.

Using Mindlin theory, we have compared the results of our experiments with the Hertz theory of elastic contact. We have compared our experimental data with the Mindlin theory of partial slip. At the lowest amplitudes we find a plateau. This plateau occurs when there is no partial slip. This is the "point contact regime" described by the Dybwad model. With increasing amplitude, we find partial slip at the rim of contact area.

High-frequency shear motion with an amplitude of 200 nm induces a strengthening of the contact. There is an increase of the Mindlin radius of contact. For glass spheres with diameter of about 700 μm, the Mindlin radius increases more than for four times. No such strengthening was found for experiment performed at amplitudes around10 nm. Smaller spheres required smaller amplitudes to induce a strengthening of the contact. To induce strengthening in a sample with spheres of smaller size needs a smaller amplitude.

At shear amplitude higher than the radius of contact, we observe the opposite effect. There very high amplitude *decreases* the Mindlin radius. Parallel to the decrease of the Mindlin radius, we observe an increase of the resistance to the shear movement. The static friction coefficient increases.

For the glass spheres, the samples in the initial state (before shear-induced strengthening) show the same behavior in increasing and decreasing drive level ramps. After strengthening of the contact the behavior becomes hysteretic. The static friction coefficient is lower in decreasing ramps than in increasing ramps. To induce partial slip at the rim of the contact, we need a high force. When decreasing the amplitude from high to low, the rim of the contact is already under slip, resulting in smaller values for the static friction coefficient.

Increasing the humidity does not have an influence on Δf_0. We do see an influence of the humidity on the partial slip length. Increased humidity decreases the partial slip length, which amounts to a decrease of the static friction coefficient. This phenomenon is caused by vapor condensation around the contact points. This water meniscus around the nanosized points of contact acts as a lubricant. When the Kelvin radius becomes comparable to the roughness of the surface, new liquid bridges form between points that initially were not in contact. The meniscus force and the water bridges make a contribution to the normal force and, as a consequence increase the shear stiffness.

Upon drying of the meniscus, we observe a large strengthening of the contacts. We termed this phenomenon sandcastle effect. As the sample dries, the radius of curvature decreases. As a consequence, the Laplace pressure (Eq. 2.11) increases. This elastically deforms surfaces into having greater area of contact and an increased number of contact points.

The increase of the contact stiffness could also be a result of salt bridges. In order to check for this hypothesis, we have made some experiments with organic solvents. The sandcastle effect for organic solvents is rather weak. The vapor pressure for ethanol and acetone is much high than for water. Therefore we have vapor condensation only for a few nanosized asperities.

It is possible do destroy the sandcastle effect with high shear amplitudes. The shear amplitudes that destroy the sphere–plate contacts depend on the size of small asperities. In order to destroy sandcastle, the average radius of small asperities must be smaller than the shear amplitude.

In some case, the stiffness of the contact was really high. A high stiffness of the contact implies a high real area of contact. With our experimental setup we can only reach small amplitudes for this sample due to the large bandwidth. We suppose that in this case of a strong sandcastle effect, the average radius of the small asperities which creates a contact is large than the maximal shear amplitude. Therefore, it is impossible to remove the sandcastle effect.

We have also investigated the radius of contact, and the static friction coefficient as a function of the normal load. There was a relaxation effect taking place after we increased the load. The characteristic time for relaxation was of 2 min.

5. Effect of high-frequency shear in adhesion force measurements

5.1. Introduction

The study of particle adhesion entered new phase with the development of the atomic force microscope (AFM). This highly sensitive instrument makes it possible to measure adhesion forces between a sharp AFM-cantilever and a surface. Attaching colloidal particles to the cantilever makes it possible to investigate the adhesion between small well defined objects and a surface.

In our work we have investigated the adhesion force with an AFM under high frequency oscillatory shear. High frequencies significantly modify the adhesion forces. This effect can not be described with the standard model. When employing high frequencies small times come into play.

In our work we have studied the dependence of the adhesion force via the pull–off–distance. We find a logarithmic dependence of the pull–off–distance while increasing the amplitude of the high-frequency shear motion. Introduction of small amounts of liquid can significantly change the physical properties of the system. Liquid increases the adhesion of the contact. Understanding of interparticle interaction is a very important step in understanding of the mechanics of the granular media.

5.2. Experimental details

The adhesion force measurements were performed by studying the detachment of an AFM cantilever from a QCM surface at high frequency shear. The solid surface used in the experiments is the gold surface of one of the electrodes of QCM or a mica sheet glued to the quartz crystal surface.

The experiments were performed with AT-cut quartz crystals with a size of 1 inch and a fundamental frequency of 5 MHz (Maxtek Inc., Santa Fe Springs, CA). The crystals were coated with gold electrodes and mounted in a home-built holder. Frequency and bandwidth were determined by the impedance analysis with an accuracy in the determination of the resonance frequency below 1 Hz. The coupling between the mechanical displacement and the

electrical via piezoelectricity makes it possible to measure the current through the electrodes (that is, the conductance) instead of measuring mechanical oscillations. It is convenient to use an equivalent circuit model to describe the electrical behavior of the QCM. In our experiments, a network analyser (HP E5100A, HEWLETT PACKARD) sweeps the frequency across the resonance and determines the admittance, $Y(\omega)$. With impedance analysis, both frequency and bandwidth were determined for the different overtones. Usually, no more than two overtones were used. All experiments were conducted at room temperature without temperature control.

A laser beam is deflected from the back of the tip and passes a knife edge on the way to the detector (see Fig. 32).

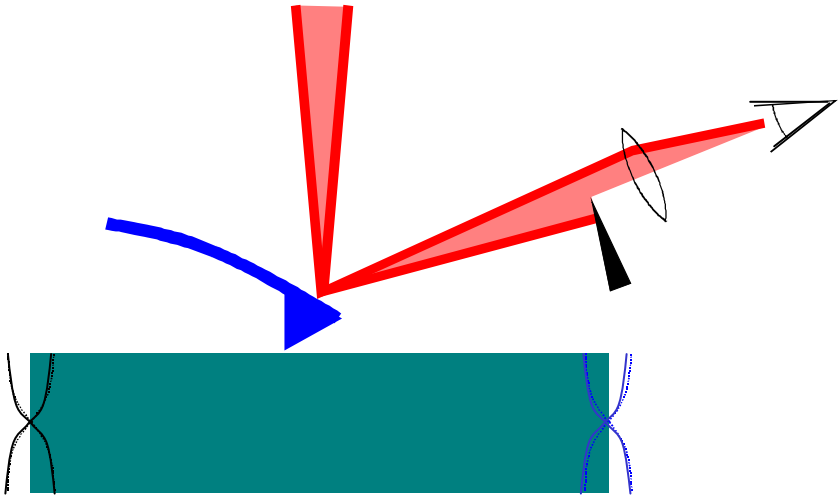

Fig. 32. Illustration of the measurement.

The output of a laser diode (Thorlabs, S1FC635, power adjustable from 0 to 3 mW, λ = 632 nm) is fed through a single-mode optical fiber. The beam exiting from the fiber is focused onto the back of the AFM-cantilever. The reflected light is directed to a knife edge, which cuts out some of the light. In the reference state, the knife edge is positioned in the centre of the optical beam. The fraction of the light which has passed the knife edge goes through a lens, which focuses the beam on the detector. As the detector, we used the PIN-diode (SSO-PDQ11.9-5-TO5, Silicon Sensor). When the AFM cantilever is deflected, the fraction of the beam passing the knife edge increases or decreases, leading to a change in intensity at the detector.

The holder with the quartz crystal was mounted on a piezo stage. The piezo stage was connected to the function/arbitrary waveform generator (Agilent 33250A). A saw tooth signal from the waveform generator provides for a vertical saw tooth movement of the crystal with

the frequency of 0.5 Hz and an amplitude of several μm. During this movement, the AFM-cantilever detaches from the surface of the quartz crystal under high frequency oscillatory shear. The pull–off–distance between the tip and the surface is the key parameter to characterize the adhesion force between the AFM-cantilever and the surface. The resonance parameters usually do not change upon contact because the tip is so small. Therefore, the experiments can be performed at one fixed frequency on the centre of the resonance.

For this measurements, we normally used AFM-cantilevers as well as cantilevers with a glass sphere glued to it. Thus, it is possible to characterize the adhesion force between the glass sphere and the surface under high frequency oscillatory shear. The glass spheres we have used had a diameter about 112 μm. It is not possible to use smaller spheres, because gluing of the spheres was done by hand. The spheres smaller than 112 μm are difficult to handle.

5.3. Mica sample preparation

In some measurements a mica sheet was glued to the top of the quartz crystal. Mica was chosen as the substrate material because the mica surface is almost atomically smooth.

A prepared mica disc with the diameter of 13 mm was placed on a normal Scotch tape. The thickness of the mica was no more than 100 μm. Before mica deposition on to the top of the QCM, the crystal was cleaned in piranha solution, rinsed in distilled water and dried. In the next steep, the crystal was heated to a temperature of ~50^{o}C for half an hour. A droplet of ~0.2 μL undiluted epoxy glue was deposited in the center of the active electrode of the QCM crystal [43] (see Fig. 33). The tape–mica sheet assembly was placed concentrically on top of the droplet, the mica side facing the glue. Capillary forces ensured spreading of the glue along the interface without entrapment of bubbles. The resin was polymerized under pressure (metal plate with the mass of several kilos) at 150°C for 1 h, after which the system was cooled overnight to room temperature and stored until use.

Before use, excess glue was scratched off around the mica sheet. The tape was peeled off, uncovering a surface of freshly cleaved mica. If necessary, the mica sheet was subsequently thinned by tape peeling until a stable oscillation of the mica-coated QCM could be obtained at several overtones in air.

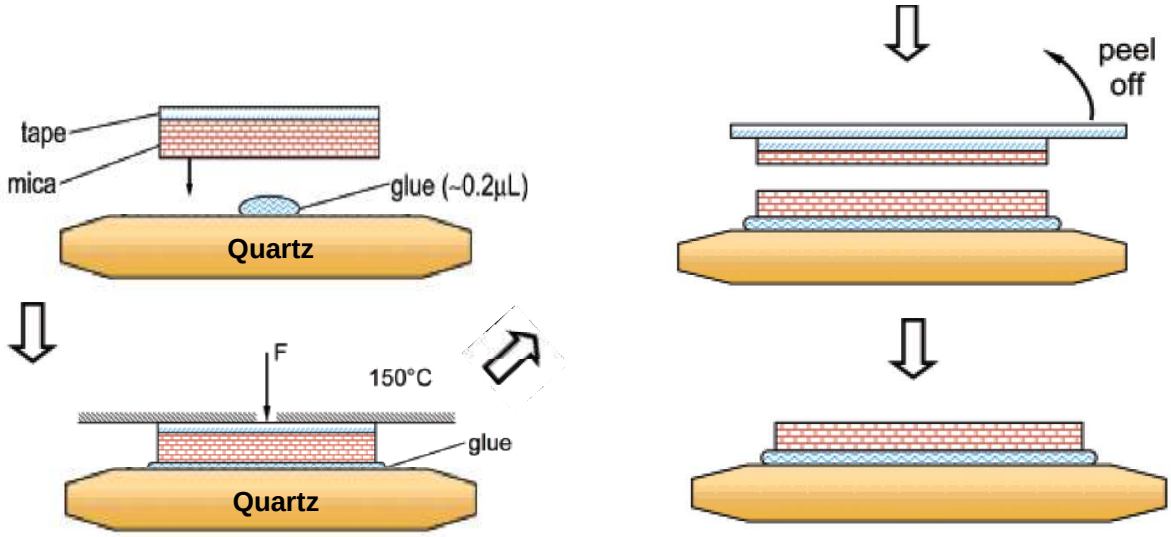

Fig. 33. Scheme of the mica sample preparation.

5.4. Detachment of an AFM cantilever from a solid surface under high frequency shear

We have carried out a set of experiments investigating the detachment of an AFM-cantilever from a solid surface in combination with high frequency shear motion. In our experiments, we have determined the pull–off–distance between the cantilever and the surface as a function of shear amplitude. The pull–of–distance is a key parameter to characterize adhesion force. We used mica samples glued to the quartz crystal surface. The reason to use mica is its atomically flat surface.

In the previous chapter, we have described the procedure of gluing mice to the quartz crystal surface. Typical conductance spectra obtained on such a sample shown in Fig. 34. These data show that, we have stable oscillations for the mica-covered crystal.

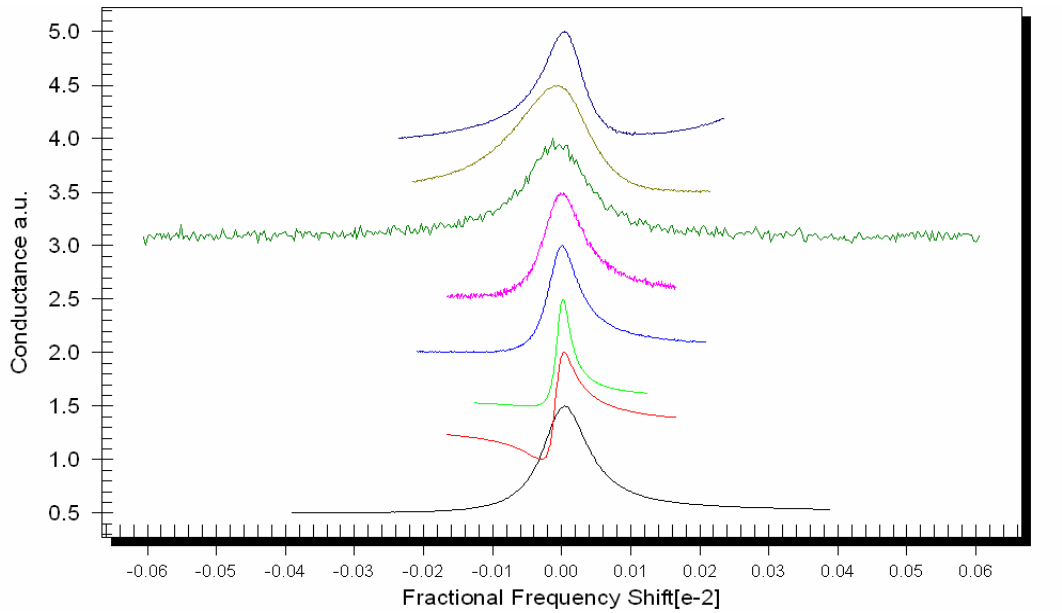

Fig. 34. Conductance spectra for a quartz crystal coated with mica. The overtone orders are (bottom to top) 5, 15, 25, …, 75 MHz.

The experimental setup was placed into a box for reasons of mechanical stability and control of humidity. Fig. 35a shows the results for the mica sample. These three measurements were performed at a frequency of 5 MHz and with a humidity of 13%.

In the results we can identify three regimes:

I. There is a plateau at the lowest amplitudes. There is no dependence on the amplitude below 0.1 nm. The shear amplitude in this stage is smaller than atomic size. This amplitude is too small to have an influence to the forces in contact area.

II. Further increasing of amplitude leads to logarithmic decrease of the pull–off–distance. In this stage, the shear amplitude decreases, the adhesion force between the AFM-cantilever and the mica surface.

III. Finally there is a saturation in the dependence of the pull–off–force on shear amplitude. A plateau result at amplitudes above 2 nm.

The dashed lines in Fig. 35 show these three regimes. Squares, triangules and circles are similar measurements with the same conditions. There show the reproducibility of the results. We did observe some hysteresis in the sense that the pull–off–distance was lowed after an amplitude sweep.

(a) *(b)*

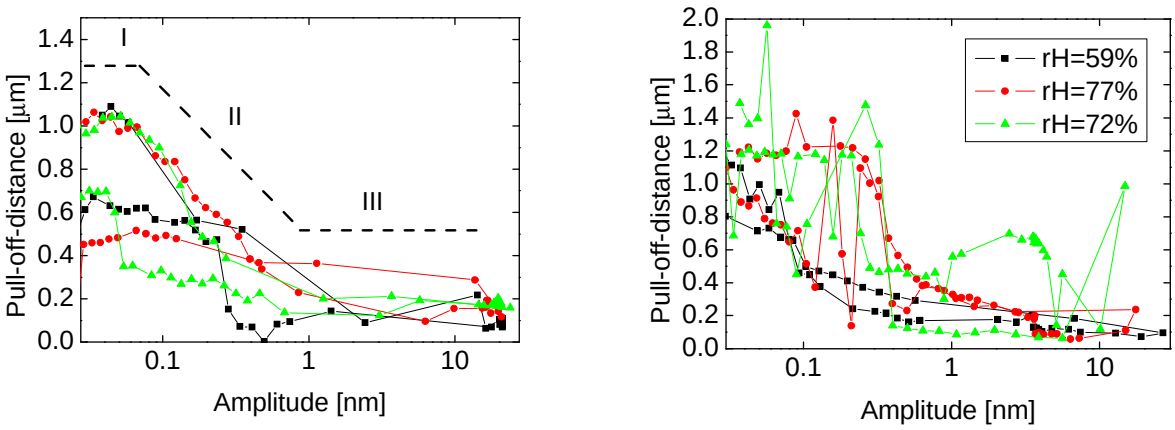

Fig. 35. Results obtained with mica-coated quartz crystal measured under high frequency (5 MHz) shear motion with Si_3N_4 AFM cantilever. (a) Three measurements with a relative humidity of 13 %rH. The dashed lines show the three regimes. (b) Measurements of a humidity of 59 %rH, 72 %rH, and 77 %rH.

Further measurements were performed with the humid air inside the box. Fig. 35*b* shows results with a relative humidity 59, 72, and 77 %rH.

Again, we can identify three regimes:

I. In the plateau range, an increase of humidity leads to increase of the pull–off–distance. The reason is an increase in the additional capillary force between the AFM-cantilever and solid surface. Fig. 36 sketches an AFM-cantilever in the dry state and in humid air. In the case of high humidity around the cantilever, we have water menisci. With increasing humidity, we have an increase in the width of the plateau. This can be also related to the water menisci. As discussed previously, high frequency shear motion from with an amplitude of 0.1 nm loosens the attachment between the AFM-cantilever and the solid surface. The presence of liquid prevents this effect.

II. The second regime corresponds to the decrease of the pull–off–distance. For the humid state we have a faster decrease of the pull–off–distance. The increase of the shear amplitude decreases the adhesion force between the AFM-cantilever and the solid surface. At the same time the shear motion destroys the menisci. The concerted action of these effects is the reason for the fast decrease of the pull–off–distance.

III. In the second plateau range we have the same conditions as for the dry state. The high amplitude shear motion destroys menisci. There is no influence of the liquid on the adhesion force.

The results shown in Fig. 35b are also nonreversible during forward and backward sweeps of amplitude. At the end of a backward sweep, we have a lower pull–off–distance than before.

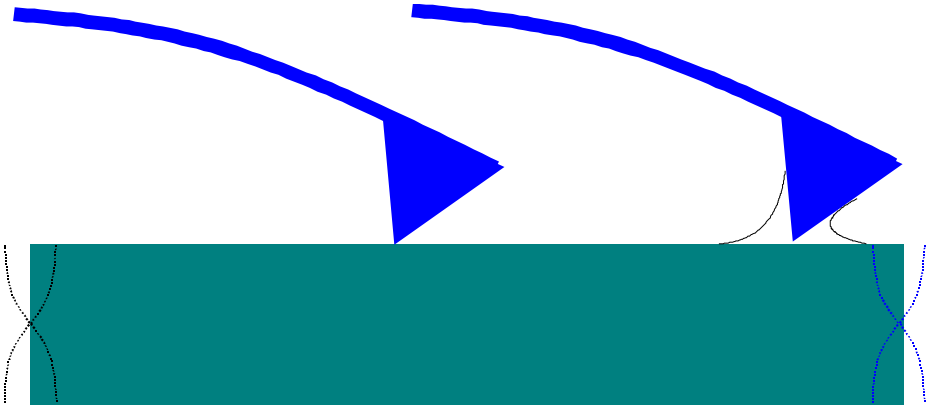

Fig. 36. Sketch to the AFM-cantilever in the dry case (left) and in the case of high humidity (right). In humid air we have menisci around the cantilever.

In regime II, we find a logarithmic decrease of the pull–off–distance with amplitude. These results are in agreement with the observations by Riedo et al. [22, 30]. These authors have studied the force of adhesion as a function of velocity with by means of AFM. Converting from speed to amplitude, their results fit the equation.

$$F_{adh} \cong A - B \ln a \qquad \text{Eq. 5.1}$$

where a is amplitude and A and B are parameters which depends on the environment. The first term, A, corresponds to the direct adhesion between the solids due to vdW forces. The second term corresponds to the capillary force (Eq. 2.14) and is a function of humidity. In our experiments we never find *increase* of the adhesion force with amplitude such an increase has also been reported in friction experiments [84, 85]. A logarithmic dependence of friction force or pull–off–force on speed vs amplitude would usually be associated with thermally activated processes (jumps of rupture of capillary bridges). Possibly, thermally activated processes can also explain our findings.

In the section 2.5 we have mentioned that there is phenomenological understanding of stick–slip motion, which connects stick–slip to an increase of the real area of contact with the time. Here, we have the reverse effect. The pull–off–force in the JKR model is proportional

to the area of contact at zero load. Interpreted in this frame, decrease of the pull–off force with amplitude implies a (logarithmic) decrease of the time–average area of contact. With increased amplitude, the area of contact logarithmically decreases.

5.5. Detachment of a glass sphere from a solid surface under high frequency shear

In previous chapter we have discussed the adhesion force between an AFM-cantilever and a solid surface. The edge of the AFM-cantilever is rather sharp. Also a field of interest is the multicontact interaction. For this reason, we have created AFM-cantilever with a glass sphere glued onto it. This way, it is possible to determine the pull–off–distance between a glass sphere a the solid surface as a function of high frequency shear amplitude.

For the experiments we have used a glass sphere with a diameter of 112 μm. In section 5.2, we have shortly described the preparation of AFM-cantilevers with a glass sphere.

Fig. 37*a* show the pull–off–distances versus shear amplitude for the mica coated quartz crystal and glass sphere. We can identify only two regimes in distinction to the AFM-cantilever where we have three regimes. The first plateau is not visible in the results with the glass sphere. If it exists, it must stop at amplitude lower than 0.1 nm.

I. The second regime shows a logarithmic decrease of the pull–off–distance with shear amplitude. This regime is much larger than with the AFM-cantilever. The decrease is observed up to an amplitude of 10 nm. In case of the glass sphere, we have a multiasperity contact.

II. The third regime, as a before, is a plateau in high amplitudes. At amplitude above 10 nm, there is no dependence on shear amplitude. The border of saturation is correlated with the roughness of the surfaces. In our case we have used mica, because it is atomically flat surface. Therefore, we have only an influence of the glass sphere roughness. The pull–off–distance on the plateau is larger than what we have for the AFM-cantilever. This is explained by the multiasperity contacts.

Contrary to the results with AFM-cantilever, we did not observe hysteretic behavior in the sense that the pull–off–distance is different for increasing and decreasing sweep. For the glass sphere, the pull–off–distance behaves reversibly in forward in backward sweeps.

(a) *(b)*

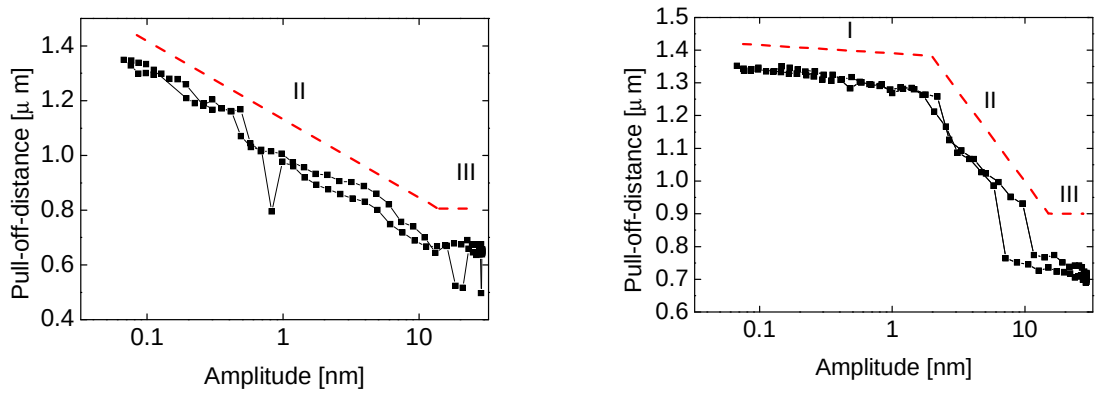

Fig. 37. The results for the mica–covered quartz crystal with a glass sphere glued to the AFM-cantilever. (a) Relative humidity of about 17 %rH. The dashed line shows the two regimes. (b)High humidity. The dashed line shows the three regimes.

In the previous measurements with the AFM-cantilevers we have increased the humidity inside the box inside which our experimental setup was placed. It is hard to keep the humidity inside the box for reason of insufficient isolation of the box and the fact that the door needs to be opened. In experiments with the glass spheres we increase the relative humidity locally near the quartz crystal with an air brush filled with water. This method is compromise. The humidity can be measured only for the whole.

Fig. 37*b* shows the pull–off–distances at high humidity. Again, there are three regimes.

I. There is a weak decrease of the pull–off–force. This regime can be identified with the plateau. The small decrease is due to multiasperity contacts. The plateau in the small amplitude regime is the result of the water bridges and menisci around contact points. The Liquid stabilizes the. In multiasperity contacts one always has points without menisci. These points establish the weak slope.

II. The pull–off–distance decreases logarithmically with amplitude. Two processes take place. Firstly, menisci are destroyed by the shear motion. Secondly the adhesion decreases under high frequency oscillatory shear.

III. The third regime is plateau. This part is the same as for dry conditions. At amplitudes above 10 nm, all menisci are destroyed. There is no influence of the liquid.

In dry state, there is no hysteresys. The pull–off–force behaves reversibly in forward and backward sweep.

The regime II is a logarithmic decrease of the pull–off distance with increase of shear amplitude. As was mentioned in this section, this regime is larger than with the AFM-cantilever. Decrease of the adhesion force between glass sphere and mica surface expressed with Eq. 5.1.

A logarithmic dependence of friction force or pull–off–force on speed on amplitude would usually be associated with thermally activated processes (jumps of rupture of capillary bridges). Possibly, thermally activated processes can also explain our findings.

In the section 2.5 we have mentioned that there is phenomenological understanding of stick–slip motion, which connects stick–slip to an increase of the real area of contact with time. Here, we have the reverse effect. The pull–off–force in the JKR model is proportional to the area of contact at zero load. Interpreted in this frame, decrease of the pull–off–force with amplitude implies a (logarithmic) decrease of the time–average area of contact. With increased amplitude, the area of contact logarithmically decreases.

The fact that regime II is larger for glass sphere, than for sharp cantilevers, may related to the area of contact. For a cantilever, the contact area is in range of several atoms. The contact between sphere and plate is made across many small asperities (multicontact interface). The area of these small asperities is larger compared to the cantilever. Consequently, the transition regime, where the true contact area decreases with amplitude can be large, as well.

5.6. Conclusion

We have performed a set of adhesion force measurements via the detachment of an Si_3N_4 AFM-cantilever from a QCM surface coated with the mica sheet. We have investigated how pull–off–distance depends on high frequency oscillatory shear in dry and wet conditions. The similar set of experiments was performed with a glass sphere glued to the AFM-cantilever.

We have found three different regimes. At small amplitudes, there is no influence of the oscillatory shear. The amplitude of shear movement is too small to have an influence on the adhesion force. This range of an amplitudes is the same for cantilever and sphere. Increasing of the humidity leads to an increase of the width of this region.

Afterwards we have a regime a decreasing adhesion force. This stage is differ out for the AFM-cantilever and the glass sphere. For the glass sphere the slope is longer. The

explanation of this effect goes back to multiasperity contact. Asperities with a larger area of contact need higher amplitudes detach force than smaller one. In high humidity, we also have a contribution from capillary forces.

In the third and last regime further increase of the shear amplitude does not decrease the adhesion force any more. The influence of the high frequency shear motion reaches a maximum. There is no dependence on humidity at these amplitudes, because the shear destroys menisci and water bridges.

6. Literature

1. D. Dowson, History of Tribology, Longman, London (1979).
2. Dahmen, S. R., H. Hinrichsen, et al. (2005). "Coupling between static friction force and torque for a tripod." Journal of Statistical Mechanics-Theory and Experiment.
3. Gao, J. P., W. D. Luedtke, et al. (2004). "Frictional forces and Amontons' law: From the molecular to the macroscopic scale." Journal of Physical Chemistry B **108**(11): 3410-3425.
4. B.N.J. Persson, Sliding friction: Physical principles and applications, Springer-Verlag Series, Berlin (1997), page 9.
5. Greenwood. Ja. and Williams.Jb (1966). "Contact of Nominally Flat Surfaces." Proceedings of the Royal Society of London Series a-Mathematical and Physical Sciences 295(1442): 300.
6. Bowden, F. P. and D. Tabor (1966). "Friction Lubrication and Wear - a Survey of Work During Last Decade." British Journal of Applied Physics 17(12): 1521-&.
7. Krim, J., D. H. Solina, et al. (1991). "Nanotribology of a Kr Monolayer - a Quartz-Crystal Microbalance Study of Atomic-Scale Friction." Physical Review Letters 66(2): 181-184.
8. Jacob Israelachvili, Intermolecular and Surface Forces, Academic Press (1985-2004)
9. Widom, A. and J. Krim (1986). "Q-Factors of Quartz Oscillator Modes as a Probe of Submonolayer-Film Dynamics." Physical Review B **34**(2): 1403-1404.
10. Daly, C., J. Krim, et al. (1992). "Applications of Atomic Scale Friction Measurements with a Quartz Crystal Microbalance." Abstracts of Papers of the American Chemical Society **203**: 290-COLL.
11. Zhong, W. and D. Tomanek (1990). "First-Principles Theory of Atomic-Scale Friction." Physical Review Letters 64(25): 3054-3057.
12. Weisenhorn, A. L., P. Maivald, et al. (1992). "Measuring Adhesion, Attraction, and Repulsion between Surfaces in Liquids with an Atomic-Force Microscope." Physical Review B 45(19): 11226-11232.

13. Cappella, B. and G. Dietler (1999). "Force-distance curves by atomic force microscopy." Surface Science Reports **34**(1-3): 1-+.

14. Sugawara, Y., M. Ohta, et al. (1993). "Effects of Humidity and Tip Radius on the Adhesive Force Measured with Atomic-Force Microscopy." Wear 168(1-2): 13-16.

15. Binggeli, M. and C. M. Mate (1994). "Influence of Capillary Condensation of Water on Nanotribology Studied by Force Microscopy." Applied Physics Letters **65**(4): 415-417.

16. Luan, B. Q. and M. O. Robbins (2005). "The breakdown of continuum models for mechanical contacts." Nature 435(7044): 929-932.

17. R. D. Mindlin and H. Deresiewicz, Journal of Applied Mechanics-Transactions of the Asme 20, 327 (1953).

18. Johnson, K. L. Kendall, K. and Roberts, A. D. “Surface energy and the contact of elastic solids”. Proc. Roy Soc., A324, pp301-320 (1971).

19. Gotzinger, M. and W. Peukert (2003). "Dispersive forces of particle-surface interactions: direct AFM measurements and modelling." Powder Technology **130**(1-3): 102-109.

20. G.A. Tomlinson, Phil. Mag. 7 (1929) 905.

21. Maeda, N., J. N. Israelachvili, et al. (2003). "Evaporation and instabilities of microscopic capillary bridges." Proceedings of the National Academy of Sciences of the United States of America **100**(3): 803-808.

22. Riedo, E., I. Pallaci, et al. (2004). "The 2/3 power law dependence of capillary force on normal load in nanoscopic friction." Journal of Physical Chemistry B **108**(17): 5324-5328.

23. Pakarinen, O. H., A. S. Foster, et al. (2005). "Towards an accurate description of the capillary force in nanoparticle-surface interactions." Modelling and Simulation in Materials Science and Engineering **13**(7): 1175-1186.

24. Orr, F. M., L. E. Scriven, et al. (1975). "Pendular Rings between Solids - Meniscus Properties and Capillary Force." Journal of Fluid Mechanics **67**(FEB25): 723-742.

25. Fisher, L. R. and J. N. Israelachvili (1981). "Experimental Studies on the Applicability of the Kelvin Equation to Highly Curved Concave Menisci." Journal of Colloid and Interface Science **80**(2): 528-541.

26. Gao, C., P. H. Dai, et al. (1998). "Meniscus forces and profiles: Theory and its applications to liquid-mediated interfaces." Journal of Tribology-Transactions of the Asme **120**(2): 358-368.

27. Christenson, H. K. (1985). "Forces between Solid-Surfaces in a Binary Mixture of Non-Polar Liquids." Chemical Physics Letters **118**(5): 455-458.

28. Xiao, X. D. and L. M. Qian (2000). "Investigation of humidity-dependent capillary force." Langmuir **16**(21): 8153-8158.

29. Jones, R., H. M. Pollock, et al. (2002). "Adhesion forces between glass and silicon surfaces in air studied by AFM: Effects of relative humidity, particle size, roughness, and surface treatment." Langmuir **18**(21): 8045-8055.

30. Riedo, E., F. Levy, et al. (2002). "Kinetics of capillary condensation in nanoscopic sliding friction." Physical Review Letters **88**(18).

31. Tocha, E., H. Schonherr, et al. (2005). "Influence of grain size and humidity on the nanotribological properties of wear-resistant nanostructured ZrO2 coatings: An atomic force microscopy study." Journal of the American Ceramic Society **88**(9): 2498-2503.

32. Bocquet, L., E. Charlaix, et al. (1998). "Moisture-induced ageing in granular media and the kinetics of capillary condensation." Nature **396**(6713): 735-737.

33. Volokitin, A. I. and B. N. J. Persson (1998). "Theory of friction: Contribution from fluctuating electromagnetic field." Physics of Low-Dimensional Structures 7-8: 17-28.

34. Persson, B. N. J. and Z. Y. Zhang (1998). "Theory of friction: Coulomb drag between two closely spaced solids." Physical Review B 57(12): 7327-7334.

35. Persson, B. N. J. and A. I. Volokitin (1995). "Electronic Friction of Physisorbed Molecules." Journal of Chemical Physics 103(19): 8679-8683.

36. Sokoloff, J. B. (1995). "Theory of the Contribution to Sliding Friction from Electronic Excitations in the Microbalance Experiment." Physical Review B 52(7): 5318-5322.

37. Sokoloff, J. B. (1998). "Effects of stick-slip motion on energy dissipation in small sliding solids." Journal of Physics-Condensed Matter 10(44): 9991-9998.

38. Mate, C. M., G. M. McClelland, et al. (1987). "Atomic-Scale Friction of a Tungsten Tip on a Graphite Surface." Physical Review Letters **59**(17): 1942-1945.

39. McMillan, A. J. (1997). "A non-linear friction model for self-excited vibrations." Journal of Sound and Vibration **205**(3): 323-335.

40. Johannsmann, D. and L. O. Heim (2006). "A simple equation predicting the amplitude of motion of quartz crystal resonators." Journal of Applied Physics 100(9).

41. K.L. Johnson: Contact Mechanics, Cambridge University Press 1985, chapter 4

42. K.L. Johnson: Contact Mechanics, Cambridge University Press 1985, chapter 7

43. Richter, R. P. and A. Brisson (2004). "QCM-D on mica for parallel QCM-D-AFM studies." Langmuir 20(11): 4609-4613.

44. Lior Kogut and Izhak Etsion, Adhesion in elastic-plastic spherical microcontact, Journal of Colloid and Interface Science 261(2003) 372-378

45. Curie J, Curie P. Développement, par pression, de l'électricité polaire dans les cristaux hémièdres à faces inclinées. Comptes Rendus de l'Académie des Sciences 1880;91:294–5.

46. Curie J, Curie P. Sur l'électricité polaire dans les cristaux hémièdres à faces inclinées. C R Acad Sci Gen 1880;91:383–6.

47. Curie J, Curie P. Contractions et dilatations produites par des tensions dans les cristaux hémièdres à faces inclinées. C R Acad Sci Gen 1880;93:1137-40.

48. Sauerbrey, G. (1959). "Verwendung Von Schwingquarzen Zur Wagung Dunner Schichten Und Zur Mikrowagung." Zeitschrift Fur Physik **155**(2): 206-222.

49. Su, X. D. and H. Zhang (2004). "Comparison of surface plasmon resonance spectroscopy and quartz crystal microbalance for human IgE quantification." Sensors and Actuators B-Chemical 100(3): 309-314.

50. Bund, A., A. Baba, et al. (2003). "Combining surface plasmon resonance and quartz crystal microbalance for the in situ investigation of the electropolymerization and doping/dedoping of poly(pyrrole)." Journal of Physical Chemistry B **107**(28): 6743-6747.

51. Coffey, T., M. Abdelmaksoud, et al. (2001). "A scanning probe and quartz crystal microbalance study of the impact of C-60 on friction at solid-liquid interfaces." Journal of Physics-Condensed Matter **13**(21): 4991-4999.

52. Berg, S., M. Ruths, et al. (2002). "High-frequency measurements of interfacial friction using quartz crystal resonators integrated into a surface forces apparatus." Physical Review E **65**(2).

53. Torbjörn Tjärnhage and Michael Sharp "The use of a quartz crystal microbalance

combined with ellipsometry and cyclic voltammetry for determining some basic characteristics of an electroactive polymer film" Electrochimica Acta 39 (1994) 623-628.

54. Torbjörn Tjärnhage (1996) “Thin Polymer and Phospholipid Films for Biosensors. Characterisation with Gravimetric, Electrochemical and Optical Methods”
55. Johannsamnn, D. „Studies of Viscoelasity and Micromechanics with the QCM“
56. Bae, S. (2005). "Long-term analysis of a swing using the two-timing method." European Journal of Physics 26(5): 791-801.
57. Dybwad, G. L. (1985). "A Sensitive New Method for the Determination of Adhesive Bonding between a Particle and a Substrate." Journal of Applied Physics **58**(7): 2789-2790.
58. Laschitsch, A. and D. Johannsmann (1999). "High frequency tribological investigations on quartz resonator surfaces." Journal of Applied Physics **85**(7): 3759-3765.
59. Berg, S. and D. Johannsmann (2003). "High speed microtribology with quartz crystal resonators." Physical Review Letters 91(14).
60. Berg, S., D. Johannsmann, et al. (2002). "Frequency response of quartz crystal shear-resonator during an adhesive, elastic contact in a surface forces apparatus." Journal of Applied Physics **92**(11): 6905-6910.
61. Berg, S., M. Ruths, et al. (2003). "Quartz crystal resonators with atomically smooth surfaces for use in contact mechanics." Review of Scientific Instruments 74(8): 3845-3852.
62. J Arnau, A., T. Sogorb, et al. (2002). "Circuit for continuous motional series resonant frequency and motional resistance monitoring of quartz crystal resonators by parallel capacitance compensation." Review of Scientific Instruments 73(7): 2724-2737.
63. J Chen, P. C. and L. Wu (2000). "The equivalent circuit of an AT-cut quartz resonator and its application." Japanese Journal of Applied Physics Part 1-Regular Papers Short Notes & Review Papers 39(5A): 2710-2713.
64. Johannsmann, D. (1999). "Viscoelastic analysis of organic thin films on quartz resonators." Macromolecular Chemistry and Physics 200(3): 501-516.
65. D'Amour, J. N., J. J. R. Stalgren, et al. (2006). "Capillary aging of the contacts

between glass spheres and a quartz resonator surface." Physical Review Letters 96(5).

66. Johannsmann, D., K. Mathauer, et al. (1992). "Viscoelastic Properties of Thin-Films Probed with a Quartz-Crystal Resonator." Physical Review B **46**(12): 7808-7815.
67. K.L. Johnson: Contact Mechanics, Cambridge University Press 1985, chapter 7.4
68. Halsey, T. C. and A. J. Levine (1998). "How sandcastles fall." Physical Review Letters 80(14): 3141-3144.
69. Hornbaker, D. J., R. Albert, et al. (1997). "What keeps sandcastles standing?" Nature 387(6635): 765-765.
70. Berthoud, P. and T. Baumberger (1998). "Shear stiffness of a solid-solid multicontact interface." Proceedings of the Royal Society A: Mathematical, Physical and Engineering Sciences 454(1974): 1615-1634.
71. Bureau, L., T. Baumberger, et al. (2000). "Shear response of a frictional interface to a normal load modulation." Physical Review E 62(5): 6810-6820.
72. Bureau, L., T. Baumberger, et al. (2001). "Low-velocity friction between macroscopic solids." Comptes Rendus De L Academie Des Sciences Serie Iv Physique Astrophysique 2(5): 699-707.
73. B. Du, D. Johannsmann, et al. “Partial Slip at Sphere–Plate Contacts Under MHz Oscillatory Shear” in preparation.
74. He, M. Y., A. S. Blum, et al. (2001). "Critical phenomena of water bridges in nanoasperity contacts." Journal of Chemical Physics **114**(3): 1355-1360.
75. Jones, R., H. M. Pollock, et al. (2002). "Adhesion forces between glass and silicon surfaces in air studied by AFM: Effects of relative humidity, particle size, roughness, and surface treatment." Langmuir **18**(21): 8045-8055.
76. Maugis D.: Contact, Adhesion and Rupture of Elastic Solids. Springer-Verlag, Berlin, 2000.
77. F.P. Bowden, D. Tabor, Friction and Lubrication, Methuen, London, 1967
78. Braun, O. M. and A. G. Naumovets (2006). "Nanotribology: Microscopic mechanisms of friction." Surface Science Reports 60(6-7): 79-158.
79. Heslot, F., T. Baumberger, et al. (1994). "Creep, Stick-Slip, and Dry-Friction Dynamics - Experiments and a Heuristic Model." Physical Review E 49(6): 4973-

4988.

80. Baumberger, T., F. Heslot, et al. (1994). "Crossover from Creep to Inertial Motion in Friction Dynamics." Nature 367(6463): 544-546.

81. Baumberger, T., C. Caroli, et al. (1995). "Nonlinear-Analysis of the Stick-Slip Bifurcation in the Creep-Controlled Regime of Dry Friction." Physical Review E 51(5): 4005-4010.

82. Greenwoo.Ja and Williams.Jb (1966). "Contact of Nominally Flat Surfaces." Proceedings of the Royal Society of London Series a-Mathematical and Physical Sciences 295(1442): 300-&.

83. Flanigan, C. M., M. Desai, et al. (2000). "Contact mechanics studies with the quartz crystal microbalance." Langmuir 16(25): 9825-9829.

84. Gnecco, E., R. Bennewitz, et al. (2000). "Velocity dependence of atomic friction." Physical Review Letters 84(6): 1172-1175.

85. Riedo, E., E. Gnecco, et al. (2003). "Interaction potential and hopping dynamics governing sliding friction." Physical Review Letters 91(8).

86. Berthoud, P., T. Baumberger, et al. (1999). "Physical analysis of the state- and rate-dependent friction law: Static friction." Physical Review B **59**(22): 14313-14327.

87. Bureau, L., C. Caroli, et al. (2006). "Frictional dissipation and interfacial glass transition of polymeric solids." Physical Review Letters 97(22).

88. Dieterich, J. H. and B. D. Kilgore (1994). "Direct Observation of Frictional Contacts - New Insights for State-Dependent Properties." Pure and Applied Geophysics 143 (1-3): 283-302.

89. Baumberger, T. and C. Caroli (2006). "Solid friction from stick-slip down to pinning and aging." Advances in Physics **55**(3-4): 279-348.

CURRICULUM VITAE

Rudenkiy S. Sergiy
Sägemüllerstr 71
Claushal-Zellerfeld 38678
Germamy

Tel: +49-5323-72-2635 (work)
e-mail: rudenkiy@gmail.com

27 years old, single

EDUCATION

1997-2003	Student of the Kharkov National University, Physical-Technical Faculty, majoring in EXPERIMENTAL NUCLEAR PHYSICS AND PLASMA PHYSICS.
2001	July 14 - 28, 2001 Summer School 2001, Institute for Nuclear Physics, Darmstadt University of Technology, Germany.
1987 - 1997	Kharkov Secondary School #62 with advanced learning of physic, mathematics and English language

Professional experience

2000 - 2003	Scientific and technological centre of Electrophysics National Academy of Sciences of Ukraine (28 Chernyshovsky Street, P.O.Box8812 UA-61002, Kharkov, Ukraine)
2003-2005	Department of Atom and Molecular physics of surface, Institut of physics and physical technology TU Clausthal Germany (AG-Kempter, IPPT TU Clausthal, Leibnizstrasse 4, Clausthal-Zellerfeld D-38678, Germany http://www.pe.tu-clausthal.de/IPPT/).“ Elektronenspektroskopische (MIES, UPS (HeI und II)) und elektronen-mikroskopische (LEEM, PEEM, STM/AFM) Untersuchungen an organisierten Nanostrukturen“ Working experience with AFM/STM, MIES/UPS.

2005-2007	Department of Polymer Interfaces, Institute of Physical Chemistry TU Clausthal Germany (Johannsmann Group, IPC TU Clausthal, Arnold-Sommerfeld-Str. 4, Clausthal-Zellerfeld D-38678, Germany http://www.pc.tu-clausthal.de/forschung/ak-johannsmann/). "High frequency contact mechanics"

PUBLICATIONS

Formation and Characterization of Pt Nanoparticle Networks

Fei Wen, Norbert Waldöfner, Wolfgang Schmidt, Klaus Angermund, Helmut Bönnemann, Stephanie Modrow, Svetlana Zinoveva, Hartwig Modrow, Josef Hormes, Lars Beuermann, Sergiy Rudenkiy, Wolfgang Maus-Friedrichs, Volker Kempter, Thomas Vad and Heinz-Günter Haubold European Journal of Inorganic Chemistry 18, 3625-3640

Interaction of O2, CO and CO2 with Co films

M. Frerichs, F.X. Schweiger, F. Voigts, S. Rudenkiy, W. Maus-Friedrichs and V. Kempter, Surface and Interface Analysis (2005)

Study of the Structure and Stability of Co Nanoparticles for Ferrofluidic Applications

S. Rudenkiy, M. Frerichs, F. Voigts, W. Maus-Friedrichs, V. Kempter et al., at Applied Organometallic Chemistry(2004)

LANGUAGES

Russian, Ukrainian	– native
English	– good
German	– basic